LBNL-47377

ERNEST ORLANDO LAWRENCE
BERKELEY NATIONAL LABORATORY

Dislocation Dynamics and Core Structure

Karin S. Lin

Materials Sciences Division
Center for Advanced Materials

May 2000

Ph.D. Thesis

DISCLAIMER

LBNL-47377

Dislocation Dynamics and Core Structure

Karin Shu Lin
Ph.D. Thesis

Materials Sciences Division
Ernest Orlando Lawrence Berkeley National Laboratory
University of California
Berkeley, CA 94720

May 2000

This work was supported by the Director, Office of Science, Office of Basic Energy Sciences, Materials Sciences Division, of the U.S. Department of Energy under Contract No. DE-AC03-76SF00098.

Dislocation Dynamics and Core Structure

by

Karin Shu Lin

B. S. (Massachusetts Institute of Technology) 1995
M. A. (University of California at Berkeley) 1998

A dissertation submitted in partial satisfaction of the
requirements for the degree of

Doctor of Philosophy

in

Physics

in the

GRADUATE DIVISION
of the
UNIVERSITY OF CALIFORNIA, BERKELEY

Committee in charge:

Professor Daryl Chrzan, Co-chair
Professor Steven Louie, Co-chair
Professor Peter Yu
Professor J. W. Morris

Spring 2000

Abstract

Dislocation Dynamics and Core Structure

by

Karin Shu Lin

Doctor of Philosophy in Physics

University of California at Berkeley

Professor Daryl Chrzan, Co-chair

Professor Steven Louie, Co-chair

Understanding the dynamics of dislocations is essential to the accurate prediction of the mechanical properties of materials. In recent years, considerable progress has been made in this area through the development of large computer simulations which seek to model plastic deformation by considering the interactions of many dislocations. However, the many-body nature of the problem, as well as the limitations inherent in the elasticity theory used to describe dislocation interactions, requires that such simulations make certain simplifying assumptions. The work reported here seeks to examine some of the issues relevant to these simulations in two ways.

First, the dynamics of a single dislocation are studied through the development and analysis of a mesoscopic, two-dimensional kinetic Monte Carlo simulation of dislocation motion. The stress and temperature dependence of the dislocation velocity is studied, and finite-size effects are discussed. Through a simple analogy to models of crystal growth, it is shown that the simulated dislocations exhibit kinetic roughening with scaling exponents predicted by the Kardar-Parisi-Zhang equation.

Second, the structure of dislocation cores is studied at the atomic level in diamond cubic materials. These studies are necessary for understanding dislocation properties at small distances, and can provide accurate parameters for use in larger scale continuum simulations. The first study uses periodic supercells and *ab initio*

techniques to compare two possible reconstructions of the 90° partial dislocation core in diamond. The relative energies are found to depend upon the stress field experienced by a dislocation in the periodic array. By fitting the energies to an isotropic elasticity theory expression for the dislocation core energy, values for the core radius and shear modulus of diamond are extracted and found to agree well with theoretical estimates and experimental observations.

A similar analysis using empirical potentials is then performed for the 90° partial dislocation in silicon. Both periodic boundary conditions and cylindrical cluster calculations are employed. The stress dependence of the relative energies of the two core reconstructions is quantified, and it is argued that one may be able to observe a transition in the stable core structure when a hydrostatic pressure is applied.

Dedication

To my husband, Cade Murray.

Acknowledgments

It is my great pleasure to thank my advisor, collaborator, and mentor, Prof. Daryl Chrzan. I have learned immensely through his guidance and encouragement not only during my dissertation research, but in all other aspects of my graduate career. He has been an inspiration to me both professionally and personally, and I am privileged to have had the opportunity to work with him.

I wish to thank Prof. Steven Louie for serving as my co-advisor as well as sitting on both my dissertation committee and qualifying exam committee, along with Prof. J. W. Morris and Prof. Peter Yu. In addition, I thank Prof. Alex Zettl for sitting on my qualifying exam committee as well as for many stimulating discussions which were instrumental in increasing my understanding of solid state physics.

I would like to acknowledge Xavier Blase, Andrew Canning, and Steven Louie for their collaboration on the diamond core structure work. Computer time provided by the National Energy Supercomputer Research Center (NERSC) for the kinetic Monte Carlo work is gratefully acknowledged. I am grateful to Ames Laboratory, funded by the U. S. Department of Energy, for providing the original AL_CMD code which was modified for the silicon core calculations. Finally, I acknowledge financial support from the U. S. Department of Energy, Office of Basic Energy Sciences, under contract DE-AC03-76SF00098.

I thank past and present students of the Chrzan research group—Lawrence Friedman, Pushkar Ranade, Tony Faradjian, Can Erdonmez, Alex Greaney, Matt Sherburne, and Chris Krenn—for useful discussions and for creating a fun and stimulating atmosphere conducive to research and learning.

I have been blessed with a wonderful group of friends who have supported me and helped me maintain perspective during difficult times. I thank Liana Seneriches for her enduring optimism and ready sense of humor, Celeste Winant for providing a welcome female presence in a male-dominated environment, and Barbara DeVolder for imparting to me her valuable insight, wisdom, and experience in all areas of life.

Finally, this work would not have been possible without the love, support, and encouragement of my parents, Chii-Dong and Shu-Mei Lin, and my husband, Cade Murray.

Contents

Chapter 1

Introduction

The mechanical properties of materials play a large role in many engineering applications. In order to determine the suitability of a given material, one must understand how that material responds to a force and how factors such as external pressure and temperature affect that response. A crystalline solid under stress can fracture, deform elastically (reversibly), or yield. In the case of yielding, plastic (irreversible) deformation occurs. Dislocations, or line defects in a crystal, are the primary agents for plastic deformation. The focus of this work is the dynamics and atomic structure of dislocations, with the goal of obtaining information that will be useful to those desiring to understand and model the mechanisms responsible for plastic deformation.

1.1 Organization

This chapter is devoted to a brief review of dislocation properties relevant to the present work and an overview of some recent work in the field of dislocation modeling. One of the ultimate goals in materials science research is to be able to predict mechanical properties of materials by considering the interaction of many dislocations. However, this involves bridging a number of length scales, from the "macroscopic" level, in which the material is treated as a continuum, through the "mesoscopic" level on which microstructural phenomena are observed, down to the

"microscopic" level of the atoms in the material. This approach is known as multiscale modeling. The first part of this work, presented in Chapter 2, attempts to address some of the issues surrounding the simulation of plastic deformation through the development and analysis of a two-dimensional kinetic Monte Carlo model for dislocation dynamics. The second part of this work, presented in Chapters 3 and 4, focuses on the atomic structure of dislocations in diamond and silicon. An attempt to link this microscopic length scale with the mesoscopic simulations is made by showing that atomic-scale calculations can be used to extract parameters useful for inclusion in these larger simulations.

1.2 Dislocations and plastic deformation

1.2.1 History

The most striking evidence that the picture of a perfect crystal is inappropriate for real materials, and the primary motivation for the development of dislocation theory, comes from a consideration of the theoretical shear strength of a perfect crystal. The force necessary to achieve plastic flow in a perfect crystal is determined by the shear stress required to move two planes of atoms past each other. In 1926, Frenkel [1] used a simple model to obtain an estimate of this critical shear stress, and found

$$\sigma_{theor} \approx \frac{\mu}{2\pi}, \tag{1.1}$$

where μ is the shear modulus of the crystal. Although later workers, using more sophisticated models, showed that the theoretical shear strength could be reduced to about $\mu/30$, these values are still in stark contrast to experimental observations which show the shear strength to be 10^{-4} μ or lower.

The large discrepancy between theoretical and experimental predictions was explained by the introduction of dislocations, one-dimensional line defects in a crystal. In 1934, the edge dislocation was proposed by Orowan [2], Polanyi [3], and Taylor [4], to be followed in 1939 with the screw dislocation proposed by Burgers [5]. As explained in detail in section 1.2.3, the presence of dislocations lowers the critical

shear stress for plastic deformation by requiring only small displacements of atoms near the dislocation line, as compared to large displacements of all the atoms in a plane for a perfect crystal.

1.2.2 Edge and screw dislocations

A crystal can deform plastically by means of slip, in which one part of the crystal is sheared with respect to an adjacent part. The boundary between the slipped and unslipped regions corresponds to the dislocation.

A dislocation is characterized by two vectors, the line direction $\boldsymbol{\xi}$ and the Burgers vector $\mathbf{b}$. The vector $\boldsymbol{\xi}$ may be taken in either direction along the line of the dislocation. The Burgers vector is determined by drawing a closed loop (called the Burgers circuit) around the dislocation. By convention, the circuit is chosen to run clockwise when viewed along the direction of $\boldsymbol{\xi}$. The same path is then traversed in a perfect crystal, and the vector required to close the loop is defined as $\mathbf{b}$.

The two types of pure dislocations are edge and screw dislocations. An edge dislocation can be thought of as a defect formed by the insertion of an extra half-plane of atoms into an otherwise perfect crystal. In an edge dislocation, $\mathbf{b}$ and $\boldsymbol{\xi}$ are perpendicular. (See Figure 1.1.) A screw dislocation is formed by making a cut partway through the crystal, then displacing one side of the crystal relative to the other side along the direction of the cut. As shown in Figure 1.2, $\mathbf{b}$ and $\boldsymbol{\xi}$ are parallel in a screw dislocation.

In general, a dislocation can have its Burgers vector at an arbitrary angle to its line direction, and is said to be *mixed*. Within isotropic elasticity theory, and for certain cases within anisotropic elasticity theory, mixed dislocations can be treated in terms of their edge and screw components.

1.2.3 Motion of dislocations

Since the introduction of dislocations, the existence of which was later confirmed by experimental observation [7, 8], the study of plasticity in crystals has been dominated by attempts to understand and model the motion of dislocations. The

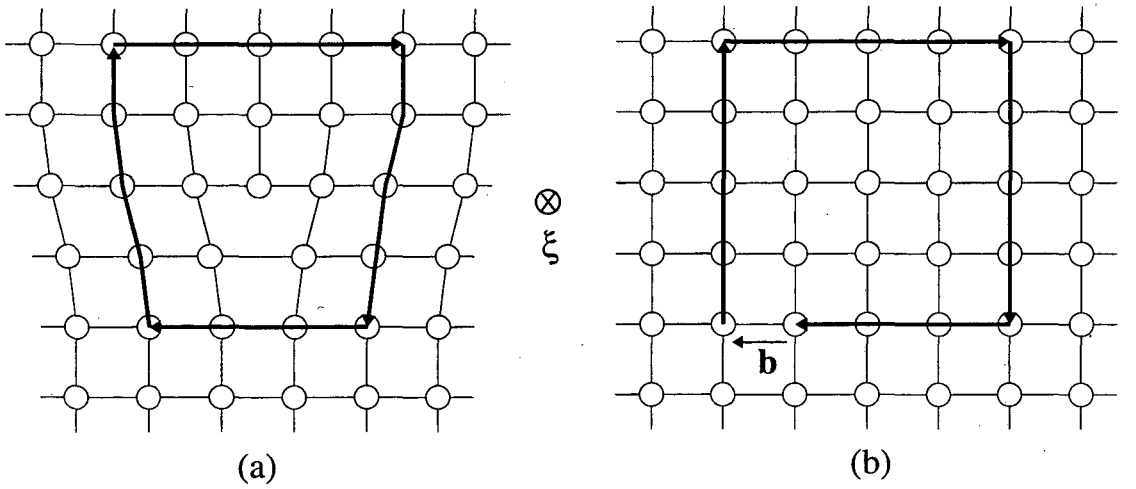

Figure 1.1: (a) Model of an edge dislocation and its corresponding Burgers circuit. (b) The same circuit in a perfect crystal, showing the closure failure **b**. From Hirth and Lothe [6].

two basic ways in which a dislocation can move are by *glide* and *climb*. In glide, the dislocation moves in a plane containing both its line direction and Burgers vector. In climb, it moves normal to this plane. Slip, or plastic deformation, occurs when many dislocations glide and one part of the crystal becomes displaced with respect to the other.

The surfaces on which the dislocations glide are called slip planes, and the direction of motion of the dislocation is called the slip direction. The slip plane in a crystal is normally the plane on which the atoms are most closely spaced, and the slip direction is the direction of closest atomic packing in that plane. In fcc crystals, for example, dislocations move in the $\langle 110 \rangle$ directions on $\{111\}$ planes.

For edge and mixed dislocations, the slip planes are uniquely defined because $\mathbf{b}$ and $\boldsymbol{\xi}$ are not parallel. The mechanism by which an edge dislocation can glide through the crystal is illustrated in Figure 1.3. The stress required to move an edge dislocation is relatively small compared to the theoretical shear strength of the crystal. For slip to be achieved in a perfect crystal, all atoms in a plane must move a lattice constant with respect to the atoms in an adjacent plane. Thus, the number of bonds

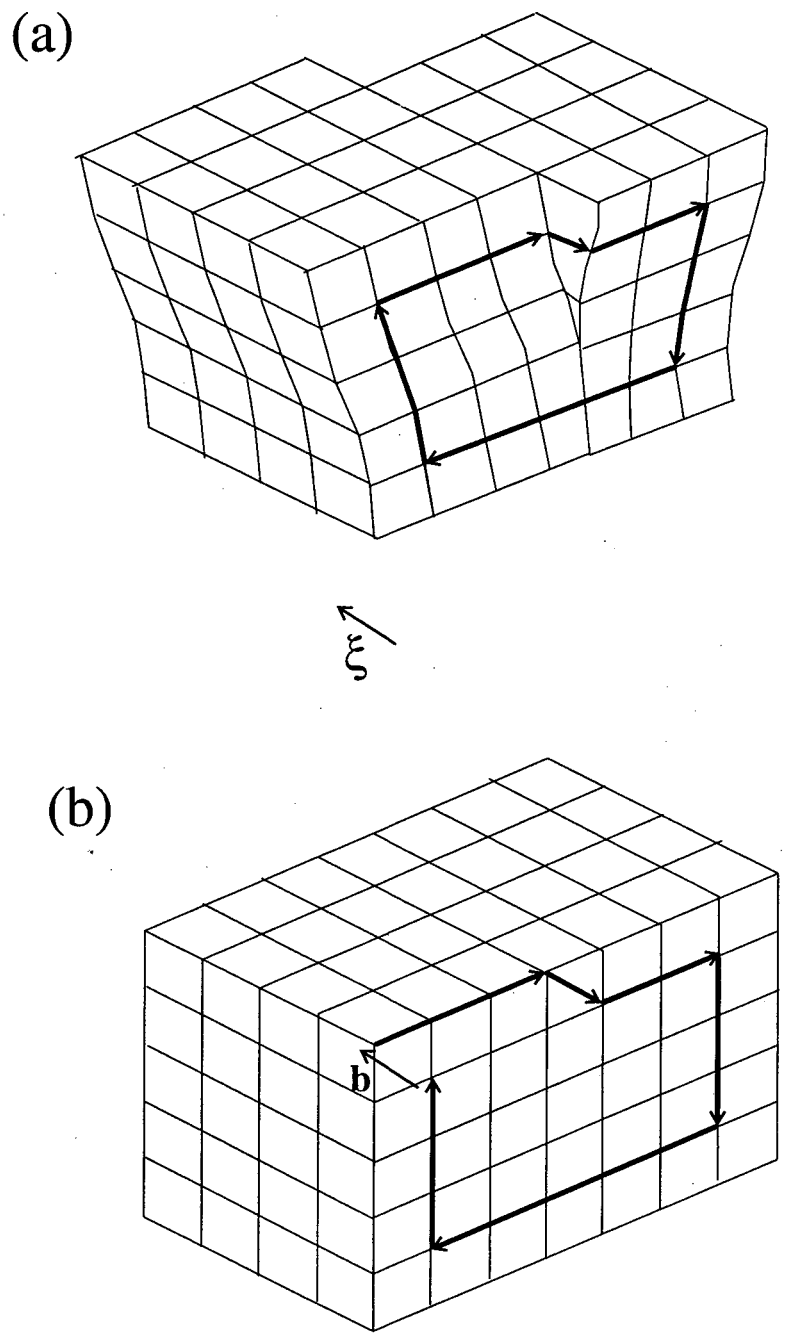

Figure 1.2: (a) Model of a screw dislocation and its corresponding Burgers circuit. (b) The same circuit in a perfect crystal, showing the closure failure **b**.

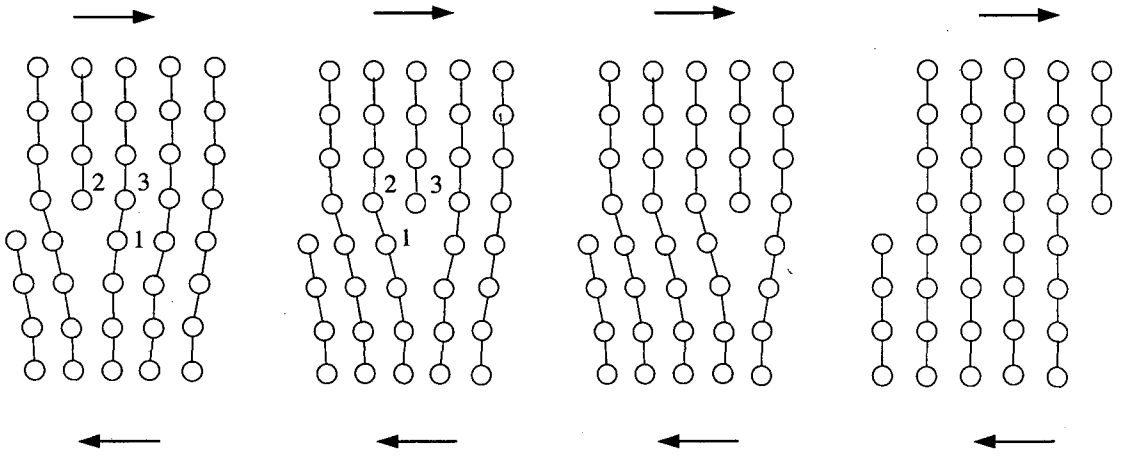

Figure 1.3: Glide of an edge dislocation through a crystal under an applied shear stress (indicated by arrows). Only atoms very near the dislocation core (*e.g.* atom 1) must move in order to advance the dislocation. From Hull and Bacon [9].

that must be broken simultaneously scales with the area of the plane. In a material containing a dislocation, however, only the atoms very near the dislocation line need move substantially. The number of bonds that must be broken thus scales with the length of the dislocation.

The movement of a screw dislocation is somewhat more difficult to illustrate, but the stress required for glide is similarly much smaller than the theoretical shear strength of the perfect crystal. A screw dislocation, however, can often move in more than one plane because its Burgers vector and line direction are parallel. In fcc crystals, screw dislocations will move in the close-packed {111} planes, but will switch from one {111} plane to the other. This process is known as cross-slip.

1.2.4 The Peierls barrier

One early attempt to quantify the contribution of dislocations to plastic deformation was made by Peierls [10] and Nabarro [11]. who estimated the stress required for dislocation glide in a periodic crystal by considering the disregistry of atoms in two semi-infinite cubic crystals, one of which contains a dislocation. As

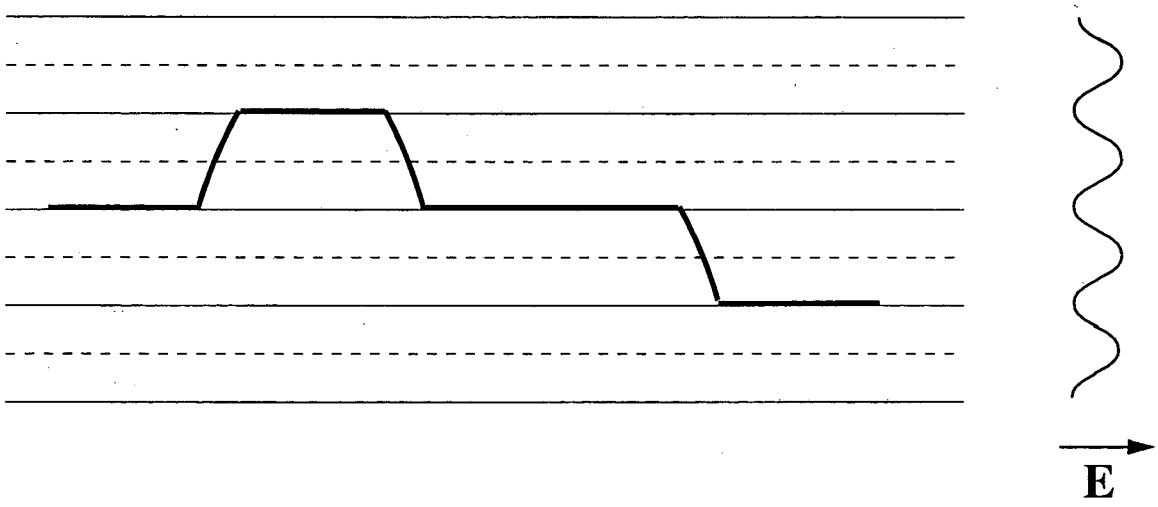

Figure 1.4: A dislocation lying primarily in Peierls energy minima.

expected, this stress (called the Peierls or Peierls-Nabarro stress) is much smaller than the theoretical shear strength of a perfect crystal. The Peierls stress is due to a potential energy (the Peierls potential or Peierls energy) experienced by the dislocation that reflects the periodicity of the crystal.

The form of the Peierls energy is ultimately determined by the atomic core structure of the dislocation, and thus an analytic expression cannot be easily derived. Peierls and Nabarro estimated the magnitude of this lattice potential by considering the disregistry of atoms in two semi-infinite cubic crystals, one of which contains a dislocation. They found that the Peierls energy per unit length was given by the expression

$$E_p = \frac{\mu b^2}{\pi(1-\nu)} \exp(\frac{-2\pi w}{b}) \tag{1.2}$$

where w, the dislocation width, is defined (somewhat arbitrarily) as the distance over which the magnitude of the disregistry between the atoms is less than half its maximum value, and is one measure of the core radius r_0 below which elasticity theory is expected to be invalid.

Although the Peierls-Nabarro model has been criticized since its introduction, and errors in the original treatment were recently described by Nabarro himself

[12], the notion that a dislocation moves in a periodic potential is important for a qualitative explanation of dislocation motion. Specifically, a dislocation will attempt to minimize its energy by lying in a Peierls valley. If it cannot lie entirely in one Peierls valley, it will contain kinks which allow it to lie in multiple valleys (see Figure 1.4). The properties of kinks and the application of kink theory to dislocation motion have been extensively studied by Seeger and Schiller [13].

The presence of kinks is central to the motion of a dislocation in a Peierls potential. In order to move a completely straight dislocation from one minimum to the next, the entire dislocation must surmount the Peierls barrier. As the temperature is increased, however, the dislocation can form oppositely signed pairs of kinks which move laterally under the application of an external stress. The energy required for this double-kink nucleation (also called kink pair nucleation) is smaller than the energy required to move the entire dislocation, since the length of dislocation moving over the Peierls barrier is shorter. In general, the stress required to move a kink laterally is smaller than the Peierls stress, and when the kinks move off the ends of the dislocation, the dislocation has advanced effectively by one lattice spacing. Figure 1.5 illustrates the motion of a dislocation via double-kink nucleation and lateral kink motion.

1.2.5 Stress field and energy of a dislocation

Within linear isotropic elasticity theory, the relationships between stress and strain are given by the equations [6, 9]

$$\begin{aligned}
\sigma_{xx} &= 2\mu\epsilon_{xx} + \lambda(\epsilon_{xx} + \epsilon_{yy} + \epsilon_{zz}) \\
\sigma_{yy} &= 2\mu\epsilon_{yy} + \lambda(\epsilon_{xx} + \epsilon_{yy} + \epsilon_{zz}) \\
\sigma_{zz} &= 2\mu\epsilon_{zz} + \lambda(\epsilon_{xx} + \epsilon_{yy} + \epsilon_{zz}) \\
\sigma_{xy} &= 2\mu\epsilon_{xy} \\
\sigma_{yz} &= 2\mu\epsilon_{yz} \\
\sigma_{zx} &= 2\mu\epsilon_{xz}
\end{aligned} \tag{1.3}$$

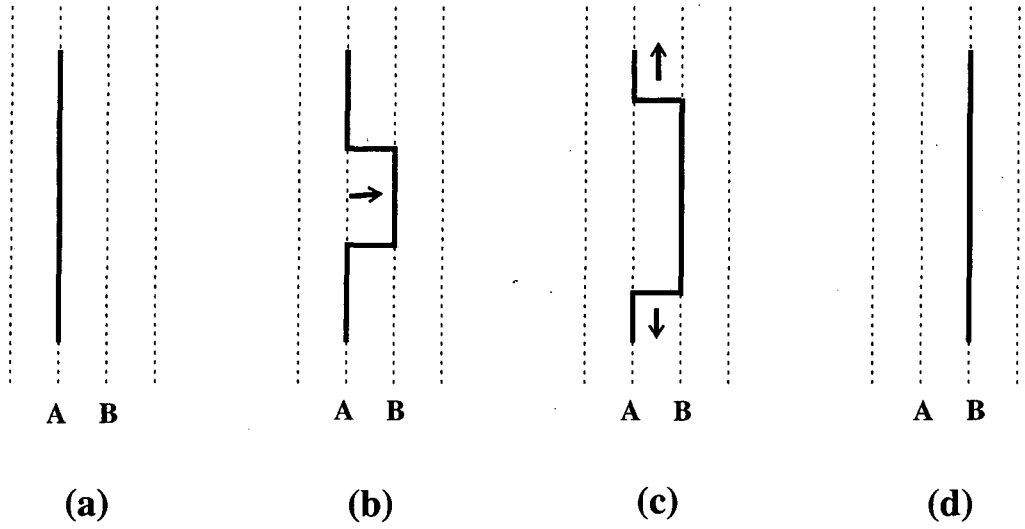

Figure 1.5: Motion of a dislocation by double-kink nucleation and lateral kink motion. (a) Dislocation begins at position A. (b) Nucleation of two oppositely signed kinks. (c) Under an external applied stress, kinks move laterally until they reach the ends of the dislocation. (d) Dislocation has advanced to position B.

where μ is the shear modulus of the crystal and λ is the Lame constant. The strains ϵ_{ij} are given in terms of the displacements u_i by

$$\begin{aligned}
\epsilon_{xx} &= \frac{\partial u_x}{\partial x} \\
\epsilon_{yy} &= \frac{\partial u_y}{\partial y} \\
\epsilon_{zz} &= \frac{\partial u_z}{\partial z} \\
\epsilon_{xy} &= \frac{1}{2}(\frac{\partial u_x}{\partial y} + \frac{\partial u_y}{\partial x}) \\
\epsilon_{yz} &= \frac{1}{2}(\frac{\partial u_y}{\partial z} + \frac{\partial u_z}{\partial y}) \\
\epsilon_{zx} &= \frac{1}{2}(\frac{\partial u_z}{\partial x} + \frac{\partial u_x}{\partial z})
\end{aligned} \tag{1.4}$$

If there are no external torques on the crystal, the stress and strain tensors must be symmetric, *i.e.*

$$\begin{aligned}
\sigma_{ij} &= \sigma_{ji} \\
\epsilon_{ij} &= \epsilon_{ji}
\end{aligned} \tag{1.5}$$

Using these relations, the stress field of an infinitely long screw dislocation can be calculated quite simply. First, the material around the dislocation is modeled by a cylinder distorted as shown in Figure 1.6. There are no displacements in the x and y directions, and in the z direction the displacement increases uniformly from 0 to b as the polar angle θ is increased from 0 to 2π. Thus,

$$\begin{aligned}
u_x &= 0 \\
u_y &= 0 \\
u_z &= \frac{b\theta}{2\pi} = \frac{b}{2\pi}\tan^{-1}\frac{y}{x}
\end{aligned} \tag{1.6}$$

From Eqs. 1.3 and 1.4, the stresses are then found to be

$$\begin{aligned}
\sigma_{xx} &= \sigma_{yy} = \sigma_{zz} = \sigma_{xy} = 0 \\
\sigma_{yz} &= \frac{\mu b}{2\pi}\frac{x}{x^2+y^2} \\
\sigma_{zx} &= -\frac{\mu b}{2\pi}\frac{y}{x^2+y^2}
\end{aligned} \tag{1.7}$$

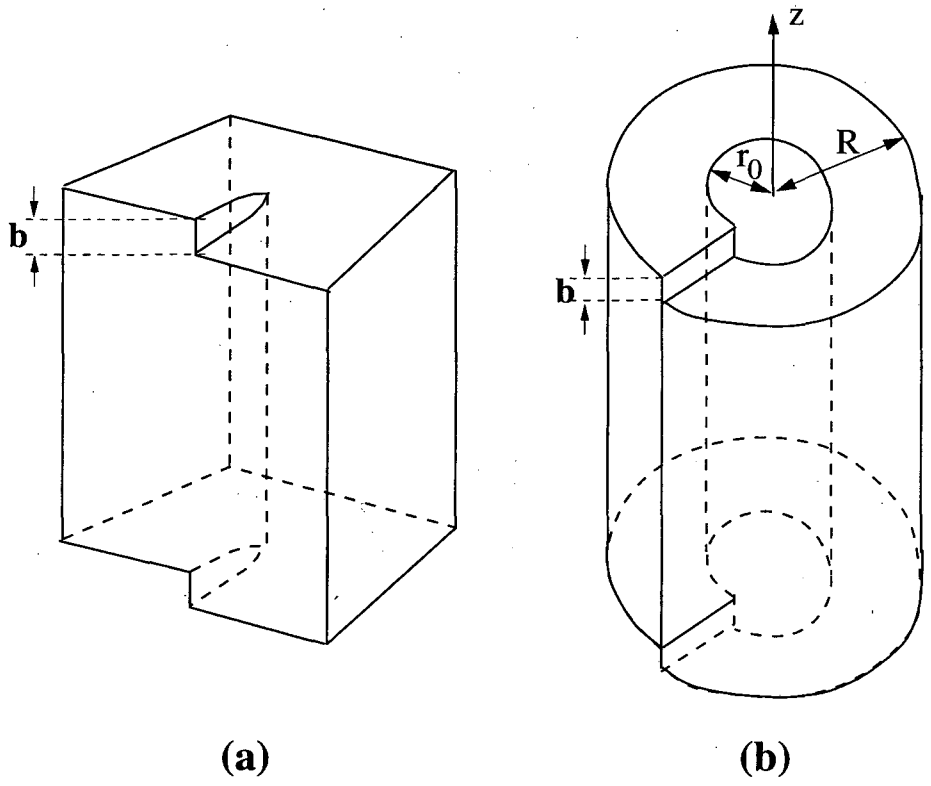

Figure 1.6: (a) Screw dislocation in a crystal. (b) Cylinder model of the elastic distortion produced by the dislocation. From Hull and Bacon [9].

The stress field of an edge dislocation is somewhat more complicated, but yields similar-looking results [6, 9]

$$\begin{aligned}
\sigma_{xx} &= -\frac{\mu b}{2\pi(1-\nu)}\frac{y(3x^2+y^2)}{(x^2+y^2)^2} \\
\sigma_{yy} &= \frac{\mu b}{2\pi(1-\nu)}\frac{y(x^2-y^2)}{(x^2+y^2)^2} \\
\sigma_{zz} &= -\frac{\mu b\nu}{\pi(1-\nu)}\frac{y}{(x^2+y^2)} \\
\sigma_{xy} &= \frac{\mu b}{2\pi(1-\nu)}\frac{x(x^2-y^2)}{(x^2+y^2)^2} \\
\sigma_{xz} &= \sigma_{yz} = 0
\end{aligned} \tag{1.8}$$

where ν is the Poisson's ratio of the solid.

Two important features of Eqs. 1.7 and 1.8 must be noted. First, the stress field of a dislocation falls off as $1/r$, where r is the distance from the dislocation. This long-range nature of the stress fields requires careful handling in both large-scale dislocation dynamics simulations and atomic scale calculations. Second, in this elasticity theory formulation the stress field diverges as $r \to 0$. This divergence is avoided by assigning a *core radius* r_0 to the dislocation. Within a distance r_0 of the dislocation, then, elasticity theory is considered to be invalid and an atomistic, non-continuum theory for the dislocation core is required.

The energy of a dislocation can be divided into two parts:

$$E = E_{core} + E_{elastic} \tag{1.9}$$

where E_{core} is the core energy of the dislocation and $E_{elastic}$ is the energy stored in the elastic stress field of the dislocation. For an infinite screw dislocation, the elastic energy per unit length $E_{elastic}/L$ may be found through a simple integration of the stress field to be

$$\frac{E_{elastic}}{L} = \frac{\mu b^2}{4\pi}\log\frac{R}{r_0} \tag{1.10}$$

where r_0 is the core radius and R is a large-scale cutoff dependent on system size. In Figure 1.6, R and r_0 are the outer and inner radii, respectively, of the cylinder. For edge dislocations, the prefactor $\mu b^2/4\pi$ is replaced with $\mu b^2/4\pi(1-\nu)$.

The division of E into the two terms in Eq. 1.9 is somewhat arbitrary, and a common convention is to incorporate E_{core} into $E_{elastic}$ by adjusting the value of the core radius r_0 [6]. This is possible because the core radius and core energy have no strict separate physical meaning; they are simply parameters inserted to make up for the failure of elasticity theory at distances very close to the dislocation line. For a given dislocation, one may thus choose $E_{core} = 0$ and replace the two parameters E_{core} and r_0 with the single parameter r_0. The core radius is often written in terms of the magnitude of the Burgers vector as as b/α, where α is a number on the order of unity [6].

In addition to the core radius r_0, there is a second parameter known as the interaction cutoff parameter ρ, which is the minimum interaction distance between two dislocation segments (*i.e.* segments do not interact when they are closer than ρ). It can be shown [6] that in order to achieve self-consistency, the quantities r_0 and ρ must be related as

$$\rho = \frac{r_0}{2} = \frac{b}{2\alpha}. \tag{1.11}$$

1.2.6 Force on a dislocation

Since the presence of a dislocation involves all the atoms in a material, it is somewhat misleading to speak of the force on a dislocation line as though the effects were entirely localized. In fact, the force on a dislocation should be considered a generalized force, as in classical mechanics, representing the change in free energy of the system when the dislocation is displaced. The displacement of a dislocation, of course, requires changes in the coordinates of all atoms in the system, and the "true" forces are distributed throughout the elastic continuum.

The force per unit length on a dislocation in the presence of a stress field can be found to be [6]

$$\frac{\mathbf{F}}{L} = (\mathbf{b} \cdot \boldsymbol{\sigma}) \times \boldsymbol{\xi}. \tag{1.12}$$

Eq. 1.12 is known as the Peach-Koehler formula [14].

As an example of the application of the Peach-Koehler formula, one may consider the force between two infinite edge dislocations of opposite sign separated

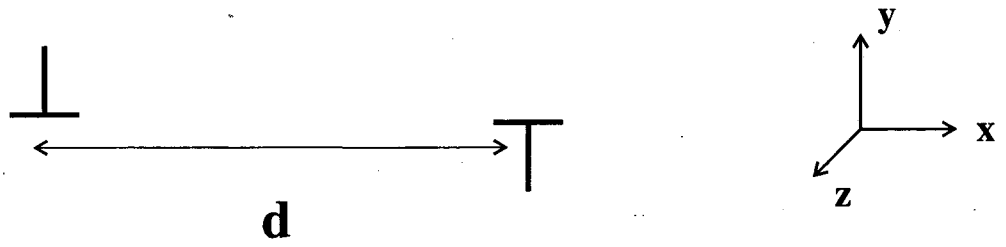

Figure 1.7: Two oppositely signed edge dislocations exert an attractive force on each other.

by a distance d, as shown in Figure 1.7. Let the left dislocation have $\mathbf{b} = b\hat{\mathbf{x}}$, $\boldsymbol{\xi} = \hat{\mathbf{z}}$, and the right dislocation $\mathbf{b} = b\hat{\mathbf{x}}$, $\boldsymbol{\xi} = -\hat{\mathbf{z}}$. Then the Peach-Koehler force on the right dislocation due to the left dislocation is just

$$F_x = b\sigma_{xy}, F_y = -b\sigma_{xx} \tag{1.13}$$

evaluated at $x = d$ and $y = 0$, where σ_{xx} and σ_{xy} are given by Eqs. 1.8. Upon substitution, F_y is found to vanish and F_x points in the $-x$ direction, implying an attractive force. In general, oppositely signed dislocations will attract, and same signed dislocations will repel.

1.2.7 Partial dislocations

The screw and edge dislocations described previously are *perfect* dislocations, which means that the Burgers vector $\mathbf{b}$ is equal to a lattice vector in the crystal. In the close-packed fcc and hcp crystal structures, however, dislocations can dissociate into *partial* dislocations, in which the Burgers vector is not equal to a lattice vector. The partial dislocations are separated by *stacking faults*, or irregularities in the order of the atomic layers.

In an fcc lattice, as previously mentioned, the predominant dislocations lie in the $\langle 110 \rangle$ directions in the $\{111\}$ slip planes. Since, according to Eq. 1.10, the energy of a dislocation is proportional to the square of the Burgers vector, it follows that the most likely Burgers vectors for a dislocation in an fcc lattice are the shortest lattice

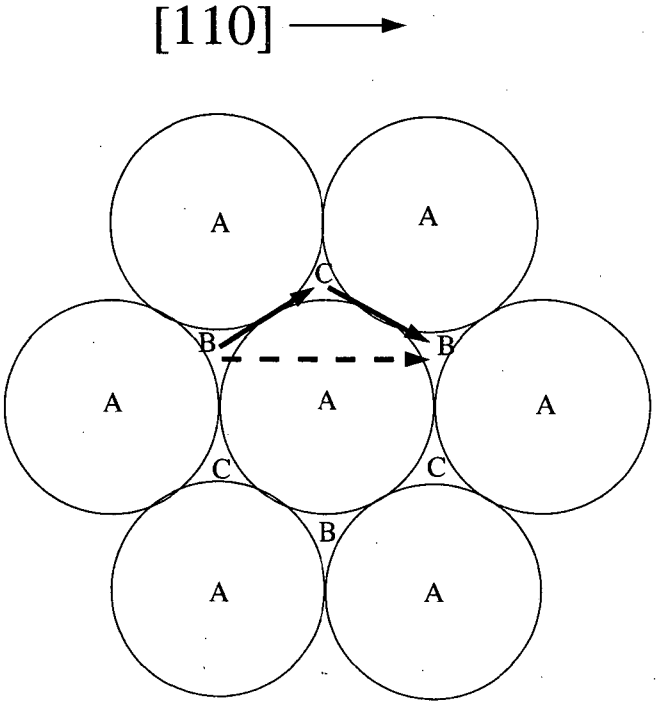

Figure 1.8: Dissociation of a perfect dislocation in the $(\bar{1}11)$ plane into two partial dislocations. From Hull and Bacon [9].

vectors in the crystal, which are of the type $\frac{1}{2}\langle 110\rangle$. An illustration of the motion of a perfect dislocation with Burgers vector $\frac{1}{2}[110]$ is given in Figure 1.8. Upon application of a shear stress to produce a displacement in the direction of slip, an atom at a site B will move in two steps, first to a nearby site C and then to the new site B. The separation of the displacement into two separate movements is represented by the dissociation of the perfect dislocation into two *Shockley partial* dislocations:

$$\frac{1}{2}[110] \rightarrow \frac{1}{6}[211] + \frac{1}{6}[12\bar{1}] \tag{1.14}$$

This dissociation is preferred because the energy associated with the single perfect dislocation is

$$E_{perfect} \propto b^2 = a^2/2 \tag{1.15}$$

whereas for the two partials

$$E_{partials} \propto b_1^2 + b_2^2 = a^2/6 + a^2/6 = a^2/3 \tag{1.16}$$

Since the energy of the two partial dislocations is lower than the energy of the perfect dislocation, the splitting is energetically favorable. The displacements associated with the two partial dislocations result in a stacking fault between them, in which the normal stacking sequence ABCABCABCABC... is replaced by ABCACABC... The separation between the two partials is determined by a balance of two forces: the force associated with the stacking fault energy, which tends to pull the dislocations together, and the elastic force which causes the dislocations to repel. Typical values of the separation in fcc metals and diamond cubic materials are on the order of 30-100 Å [15, 16, 17].

1.3 Motivation for the current work

The rapid growth of computer power in recent years has prompted several attempts to develop large-scale models of plastic deformation. Kubin and co-workers developed a 3-D mesoscopic simulation of the dynamics of large numbers of dislocations in fcc crystals [18], later extended to bcc [19] and silicon [20] crystals. Schwarz [21] has also developed a simulation of interacting dislocations, but with careful consideration of classic problem of the divergence of the self-interactions. Rhee *et al.* [22], Ghoniem *et al.* [23], and Faradjian *et al.* [24] have also produced similar models.

The simulations described above are based on elasticity theory, in which the dislocation is considered to reside in a continuous medium. While elasticity theory is adequate for most aspects of dislocation simulation (and for describing many properties of dislocations), it fails to describe the dislocation completely because the elastic self-energy of a dislocation diverges. The accurate simulation of dislocation interactions is fraught with other difficulties, such as the long range of dislocation stress fields and the effect of free surfaces on the dislocation mobility.

The essential features of these large-scale simulations are identical: All of them perform a discretization of space (and often time), model the dislocation as

a series of straight segments (with the exception of Ghoniem *et al.* [23], who use curved segments), and evolve the dislocation according to a mobility law which can depend on the elastic properties of the material, an externally applied stress, and the temperature of the sample. Central to the determination of such a mobility law, however, is an understanding of how a single dislocation propagates under an applied stress. This is the motivation for the first project described in this work: a mesoscopic kinetic Monte Carlo simulation which explores the dynamics of a single dislocation bounded by free surfaces. The second part of this work is dedicated to exploring the atomic structure of a dislocation core, information that can both provide accurate parameters for mesoscopic simulations and enable the proper treatment of a dislocation at length scales where elasticity theory breaks down.

Chapter 2

Simulation of Dislocation Dynamics[†]

The ability to model the mechanical properties of materials is of obvious practical and theoretical interest. An understanding of the processes underlying plastic deformation must, in turn, include a predictive description of dislocation dynamics. However, since dislocation densities (the number of dislocation lines that intersect a unit area in a crystal) can be as large as 10^{11} or 10^{12} dislocations/cm^2 in heavily deformed metals [26], such a description involves solving a complicated many-body problem. In recent years, several workers [18, 21, 22, 23] have attempted to address this problem by creating large continuum simulations of dislocation dynamics. But computational limits, as well as the difficulties inherent in bridging the many length scales that come into play, require the use of many approximations.

At the core of any dislocation dynamics simulation, and the goal of the work described in this chapter, is an understanding of how a single dislocation responds to an applied stress. The hope is that focusing on this smaller problem will allow a more thorough examination of the issues relevant to larger scale simulations. In particular, it is found that

- The presence of free surfaces may have a substantial effect on the dislocation velocity.

[†]The research presented in this chapter has been published in Ref. [25].

- The dislocation velocity depends on temperature differently depending on the magnitude of the applied stress.
- The dislocation exhibits kinetic roughening with exponents predicted by an analogous crystal growth problem.

2.1 The model

The full model used to obtain most of the results discussed in this chapter incorporates much detail in the calculation of elastic interactions between dislocation segments, and proves to be too computationally intensive for examination of certain phenomena. Thus, for some of the calculations, simplifications to the model are introduced which are expected not to influence the results too heavily for the quantities of interest. The full model is presented here first, and approximations will be described when their need arises in later discussion.

2.1.1 Representation of the dislocation

The dislocation is modeled as a system of pure screw and pure edge segments on a 2-D rectangular lattice. Screw segments are assumed to lie in Peierls minima, and edge segments are present only as kinks. The lattice is infinite in the direction of motion and bounded by free surfaces in the direction perpendicular to motion (see Fig. 2.1).

Since this model treats only a single dislocation and is restricted to a two-dimensional treatment, it is not expected to reproduce quantitatively the experimental observations of real materials. Nonetheless, it is useful to choose a realistic system from which to extract parameters such as atomic distances and elastic constants. The (110) slip system of tantalum is a reasonable choice since the Peierls potential is expected to be significant in bcc metals and dislocations do not dissociate into partials as in the fcc and diamond structures, thus increasing the validity of the pure screw/edge approximation.

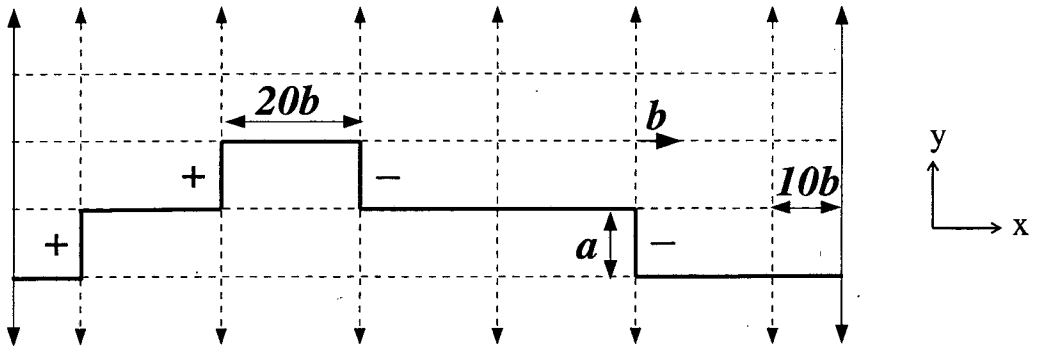

Figure 2.1: Discrete model of a dislocation (drawing not to scale). Screw segments lie in Peierls minima and edge segments are present only as kinks. The + and − signs indicate positive and negative kinks, respectively. The discretization distance in the x direction is halved at the surfaces to allow nucleation and annihilation of single kinks, thus minimizing the effects of the surfaces.

The Burgers vector b in the (110) slip system of tantalum is $a_0\sqrt{3}/2 = 2.62$ Å, where $a_0 = 3.03$ Å is the lattice constant. (See Figure 2.2.) The interaction cutoff parameter ρ (described in Section 1.2.5) is chosen to be $b/8$, corresponding to $\alpha = 4$. The discretization distance in the direction of motion is simply the distance between neighboring Peierls valleys, $a = (2/3)^{1/2}a_0 = 2.14$ Å. The discretization distance in the direction perpendicular to motion, identified with the distance of separation between kink pairs, presents a greater difficulty. The nearest neighbor distance along a Peierls valley is b. However, because oppositely signed edge dislocations attract (see section 1.2.6), kink pairs are not stable unless their separation exceeds a minimum distance which is dependent on the applied stress [6]. Incorporating this variable stress-dependent kink separation into the simulation while at the same time maintaining detailed balance is nontrivial, and failure to maintain detailed balance can lead to serious artifacts in the dislocation's structure. Therefore, the present treatment chooses to maintain detailed balance while sacrificing other physical detail. In particular, the kink separation distance is chosen to be $20b$, which gives stable kink pairs in the stress and temperature ranges of interest, and a kink migration energy (described in the following section) is added to account for the entropic contribution

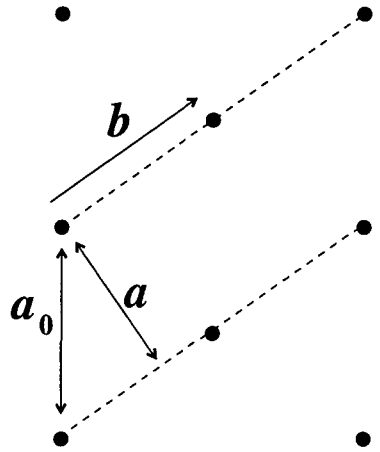

Figure 2.2: (110) slip system of a bcc metal. The dotted lines correspond to Peierls valleys.

due to the fact that "real" kinks move in steps of b. The dislocation is placed under an applied external stress σ_{xy}, which tends to move screw segments in the $+y$ direction and edge segments in the $\pm x$ direction, depending on the sign of the kink.

2.1.2 Dislocation evolution

Evolution of the dislocation is controlled by kinetic Monte Carlo procedure [27], in which the simulation proceeds by event, not by time. At each stage of the simulation, the following steps are performed.

1. A finite number of possible events is tabulated.

2. Rates R_i for the occurrence of each event are determined.

3. The time until the next event occurs is determined by the equation

$$\tau = -\frac{\ln r}{R} \tag{2.1}$$

where r is a random number between 0 and 1 and R is the sum of the individual rates R_i.

4. The actual event which occurs is chosen randomly, using the R_i as weighting factors.

5. The system is evolved to a new state determined by the chosen event.

The dislocation begins as a perfectly straight, single screw-oriented segment. At each stage of the simulation, the possible events at a given site on the dislocation may include double-kink nucleation, annihilation of an existing kink pair, or lateral motion of a single kink. The equivalent of the solid-on-solid condition for crystal growth is imposed; kinks of like sign may not approach closer than the discretization distance $20b$, thus preventing "overhangs" and extended edge segments of length greater than a. To minimize surface effects, nucleation and annihilation of single kinks are allowed to occur at a distance of $10b$ from the surface. Both events that move the dislocation in the $+y$ direction favored by the stress and events that move it in the $-y$ direction against the stress are allowed, since thermal fluctuations can overcome the additional energy bias caused by the stress.

The event rates are calculated according to the formula

$$R = \omega_o \exp(-\Delta E_{barr}/k_B T) \tag{2.2}$$

where ω_o is an attempt frequency and ΔE_{barr} is the energy barrier associated with moving between the initial and final (if the event were to occur) configurations. The attempt frequency ω_o sets the overall time scale for the evolution of the dislocation, and is typically on the order of the Debye frequency, 10^{-12} to 10^{-13} s^{-1}. A more quantitative estimate can be made by considering the Granato-Lücke model [28], which treats a dislocation as a vibrating string. The attempt frequency is chosen to be the fundamental mode of a vibrating string with length $20b$, the double-kink separation distance. Then,

$$\omega_o = C_t \pi/(20b) \tag{2.3}$$

where $C_t = 2060$ m/s is the speed of sound in tantalum, which gives

$$\omega_o = 1.23 \times 10^{12}\ s^{-1}. \tag{2.4}$$

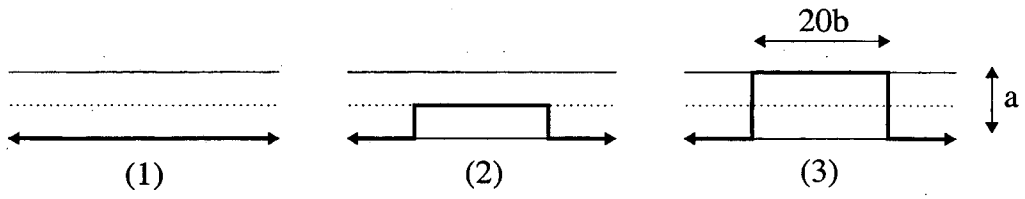

Figure 2.3: ΔE_{mid} is the energy required to pass from (1) to (2); ΔE_{final} is the energy required to pass from (1) to (3). Only the section of the dislocation in the vicinity of the nucleation site is shown.

For double-kink nucleation and annihilation, ΔE_{barr} in Eq. 2.2 is determined by comparing the energies ΔE_{mid} and ΔE_{final}. ΔE_{mid} is the energy required to nucleate a kink pair "halfway", so that the screw segment separating the kinks lies along a Peierls maximum, and ΔE_{final} is the energy required to nucleate a full kink pair. (See Figure 2.3.)

The work done by or against an applied stress σ is equal to $\pm\sigma bA$, where A is the area swept out by the dislocation. Thus

$$\Delta E_{mid} = \Delta E_P + \Delta E_{s,elastic}(\text{config}, a/2) \pm \sigma b(20b)(a/2) \tag{2.5}$$

and

$$\Delta E_{final} = \Delta E_{s,elastic}(\text{config}, a) \pm \sigma b(20b)(a). \tag{2.6}$$

where ΔE_P is the Peierls energy barrier and $\Delta E_{s,elastic}(\text{config}, y)$ is the elastic energy required to move a screw segment a distance y and *depends on the entire dislocation configuration.*

The Peierls energy ΔE_P can be determined from the Peierls stress σ_P. Experimental measurements and theoretical estimates of the Peierls stress in tantalum cover a wide range, from 340-1100 MPa [10, 11, 29, 30]. For these simulations, σ_P is chosen to be 750 MPa, corresponding to $\Delta E_P = 0.44$ eV for a screw segment of length $20b$.

Once ΔE_{mid} and ΔE_{final} are calculated,

$$\Delta E_{barr} = \begin{cases} \Delta E_{mid} & \Delta E_{mid} \geq \Delta E_{final} \text{ and } \Delta E_{mid} > 0 \\ \Delta E_{final}/2 & \text{otherwise} \end{cases} . \tag{2.7}$$

One might naturally expect ΔE_{barr} always to be defined by ΔE_{mid}, since the Peierls potential has a maximum at the halfway point. However, the Peierls energy is not always the dominating factor in the energy barrier. In some cases, the elastic energy required to move a screw segment to its final position exceeds that required to move it to the halfway position by an amount greater than the Peierls energy. Also, when the applied stress is large, double-kink nucleation is so favorable that the energy barrier is negative, and the screw segment will move immediately to its final position. Figure 2.4 illustrates schematically the ways in which the energy barrier depends on the distance y traveled by the screw segment. An ideal calculation would take into account the analytical forms of the three contributions to the energy barrier—the elastic energy, Peierls energy, and work due to applied stress—as continuous functions of the screw segment position, and calculate the maximum barrier exactly. However, the complexity of the elastic energy calculation, as well as its dependence on the entire dislocation configuration, makes such a calculation computationally unfeasible. This scheme, in which the energy barriers for only the halfway position and final position are calculated, allows for a more accurate choice of ΔE_{barr} without sacrificing computational efficiency. The factor of 2 must be added to ΔE_{final} to ensure that detailed balance is obeyed.

The energy barrier for lateral kink motion is simply

$$\Delta E_{barr} = \Delta_{mig} + \frac{1}{2}(\Delta E_{e,elastic}(\text{config}, 20b) \pm \sigma b(20b)a) \tag{2.8}$$

where Δ_{mig} is a kink migration energy and $\Delta E_{e,elastic}(\text{config}, x)$ is the elastic energy required to move an edge segment a distance x. Again, a factor of 2 (absorbed into Δ_{mig}) is added to ensure that detailed balance is obeyed.

The kink migration energy, Δ_{mig}, can be thought of as a secondary Peierls barrier in the direction of motion of the kinks, *i.e.* the $\pm x$ direction. Essentially, Δ_{mig} is added to account for the difference between simulation and reality in its discretization of space. Whereas real kinks move through barriers with a periodicity of b, kinks in the simulation must move in steps of $20b$, and there should thus be an entropic contribution to the energy barrier for this process. Δ_{mig} is a construct which allows tuning of the relative rates of kink motion and double kink nucleation/annihilation,

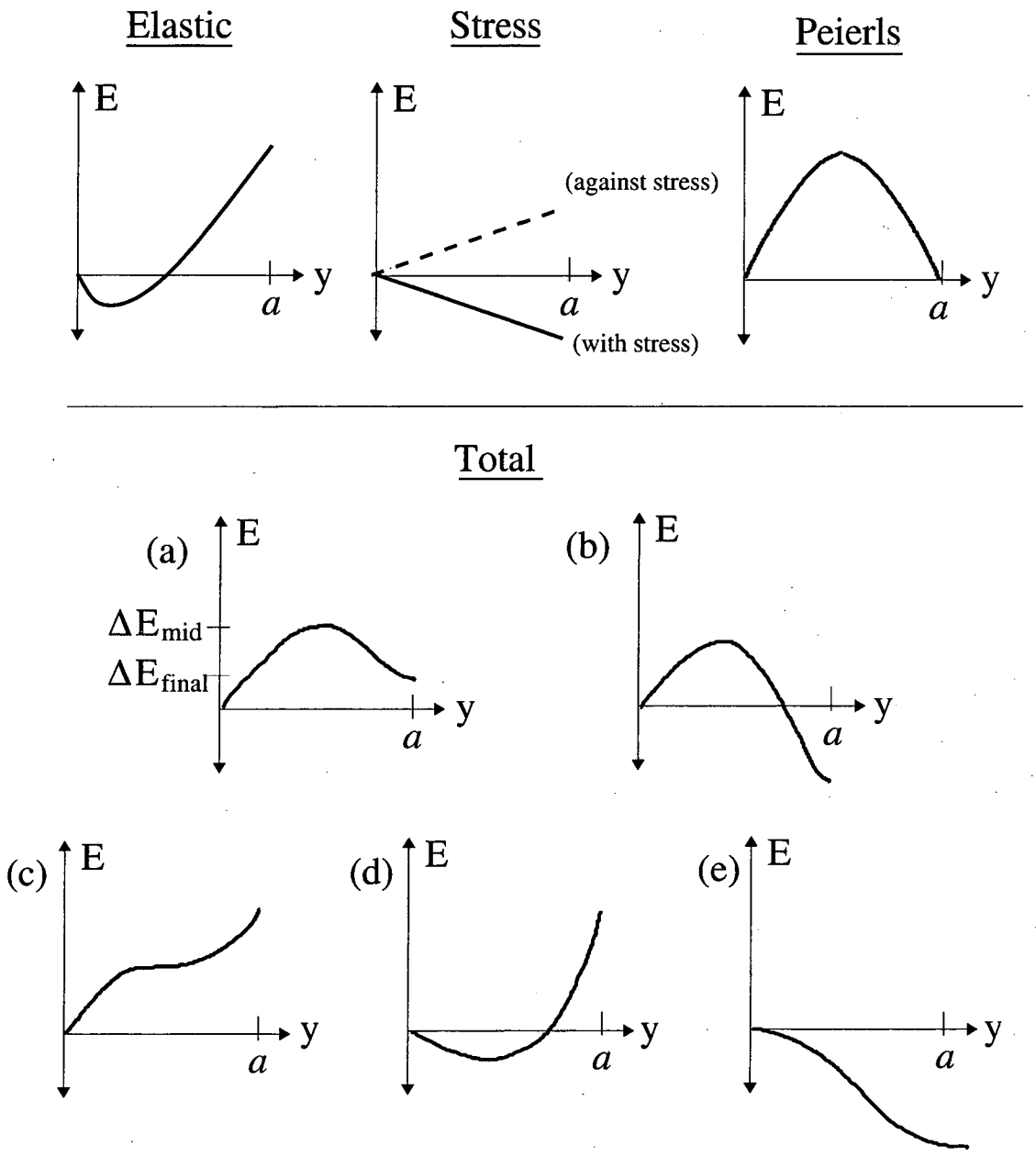

Figure 2.4: Schematic illustration of the energy barrier to double-kink nucleation, as a function of the kink height y. The form of the total energy barrier depends on the relative contributions of the elastic energy, work done by or against the applied stress, and Peierls energy. In cases (a) and (b), ΔE_{mid} is used; in cases (c), (d), and (e), $\Delta E_{final}/2$ is used. (See Eq. 2.7.)

and the value Δ_{mig}=0.25 eV is chosen so that the rates of these two types of events are comparable. Experimental observations of dislocations with low kink mobility [17, 31] suggest that this choice is not unreasonable.

The terms in Eqs. 2.7 and 2.8 have now all been defined except for the elastic energy terms, $\Delta E_{s,elastic}(\text{config}, y)$ and $\Delta E_{e,elastic}(\text{config}, x)$. In the coordinate system of Figure 2.1, the only relevant component of the stress tensor is σ_{xz}. By the Peach-Koehler formula (Eq. 1.12), it is this component that produces a force in the y direction for the screw segments ($\mathbf{b} = b\hat{\mathbf{x}}$, $\boldsymbol{\xi} = \hat{\mathbf{x}}$) and in the x direction for the edge segments ($\mathbf{b} = b\hat{\mathbf{x}}$, $\boldsymbol{\xi} = \pm\hat{\mathbf{y}}$). The value for σ_{xz} must be obtained by a sum over all the contributions from the other screw and edge segments in the dislocation. Though computationally intensive, these calculations are straightforward. The stress field $\sigma^d_{xz}(x, y)$ of a dislocation segment according to isotropic elasticity theory is well-known [6, 32]. For a screw segment lying on the x-axis between x_1 and x_2,

$$\sigma^d_{xz}(x, y) = \frac{\mu b}{4\pi} y \left[\frac{1}{r_1(r_1 - x + x_1)} - \frac{1}{r_2(r_2 - x + x_2)} \right] \tag{2.9}$$

where $r_i = ((x - x_i)^2 + y^2)^{1/2}$. For an edge segment lying on the y-axis between y_1 and y_2,

$$\sigma^d_{xz}(x, y) = \frac{-\mu b}{4\pi(1 - \nu)} x \left[\frac{1}{r_1(r_1 - y + y_1)} - \frac{1}{r_2(r_2 - y + y_2)} \right] \tag{2.10}$$

with $r_i = (x^2 + (y - y_i)^2)^{1/2}$.

To account for the presence of the free surfaces that bound the dislocation, image stresses and surface traction terms (more accurately, stress fields that annul the surface tractions) must also be considered in the calculation. The image stresses $\sigma^i_{xz}(x, y)$ are easily determined from the real stresses by transforming the coordinate system and changing the sign of the Burgers vector. The surface traction terms have also been calculated explicitly [33, 34]. For a screw segment, this term is, with $x = 0$ taken at the surface,

$$\sigma^s_{xz}(x, y) = \frac{-\mu b}{2\pi(1 - \nu)} y \left[(1 - \nu)(P_1 - P_2) - \frac{3x_1 x(x + x_1)}{r_1^5} + \frac{3x_2 x(x + x_2)}{r_2^5} \right] \tag{2.11}$$

where $r_i = ((x + x_i)^2 + y^2)^{1/2}$ and $P_i = 1/(r_i(r_i + x + x_i))$. For an edge segment a

distance c to the right of a surface at $x = 0$, the corresponding term is

$$\sigma^s_{xz}(x,y) = \frac{-\mu bc}{2\pi(1-\nu)}\left[-(P_1 - P_2) - 3x(x+c)(q_1 - q_2) + (x+c)^2(s_1 - s_2)\right] \quad (2.12)$$

with the definitions

$$\begin{aligned} r_i &= ((y-y_i)^2 + (x+c)^2)^{1/2} \\ P_i &= 1/(r_i(r_i - y + y_i)) \\ q_i &= \frac{2r_i - y + y_i}{r_i^3(r_i - y + y_i)^2} \\ s_i &= \frac{3x(x+c)}{r_i^2 - (y-y_i)^2}\left[\frac{y-y_i}{r_i^5} + \frac{4}{3}q_i\right]. \end{aligned} \quad (2.13)$$

Properly, the consideration of the surfaces requires an infinite sum over all reflections of the images on both surfaces. However, the interactions drop off rapidly as functions of both the distance from the surface of the stress-generating segment and the distance between the segment and the point of evaluation, and are significant only for segments very near the surface. Thus, only the first term in the sum is included for each segment with each surface. Furthermore, a dislocation segment with an endpoint at the surface will have that endpoint adjusted by the interaction cutoff parameter ρ to avoid a divergence in the energy.

Once the stress fields associated with all segments of the dislocation have been determined, the work required to transform a dislocation from its initial to its final configuration against these stress fields can be determined by integration. The energy required to move a screw segment against the stress fields of the other segments in the dislocation is

$$\Delta E_{s,elastic} = -b\int_{y_o}^{y_f} dy \int_{x_o}^{x_f} dx \sum_i \sigma_{xz,i} \quad (2.14)$$

where x_o and x_f are the endpoints of the screw segment, y_o and y_f are the initial and final positions of the segment, and $\sigma_{xz,i}$ is the total contribution to σ_{xz} from segment i (which can be either screw or edge) in the dislocation. This is given by

$$\sigma_{xz,i} = \sigma^d_{xz,i} + \sigma^i_{xz,i} + \sigma^s_{xz,i} \quad (2.15)$$

which is determined from Eqs. 2.9–2.13 with appropriate coordinate transformations. The equation for $\Delta E_{e,elastic}$ has an identical form, but with a different interpretation of the parameters: y_o and y_f are the endpoints of the edge segment, and x_o and x_f are its initial and final positions.

One final complication to the above expression must be considered. The movement of a screw segment in double-kink nucleation (annihilation) is accompanied by the creation (annihilation) of two new edge segments. The work done against the stress fields of these segments must also be included. This is done by using Eqs. 2.10 and 2.13, but with one of the endpoints (either y_1 or y_2, depending on the segment) replaced by the integration variable y in Eq. 2.14. Since the stress field will diverge at the "corner" where the screw segment and the new edge segment meet, one must also adjust the screw segment endpoints x_o and x_f by the interaction cutoff parameter ρ as appropriate. In the case of lateral kink motion, the screw segments adjacent to the moving edge segment will lengthen or shorten in the process and are treated in an analogous manner.

2.2 Dislocation velocity

2.2.1 Finite-size effects

Because the computational demands of the simulation place a limit on the dislocation length that can be considered, it is crucial to examine the effects of finite size, particularly with regard to the presence of the free surfaces that bound the dislocation. Further, dislocations in nature are often bounded by surfaces or interfaces. These defects may influence the dislocation velocities. In order to study the dependence of the steady-state dislocation velocity on dislocation length, a simpler model is used in which only two elastic energies are calculated, that associated with nucleating a kink pair and that associated with moving a single kink in the middle of an otherwise flat dislocation. These two quantities then replace the configuration-dependent terms in Eqs. 2.7 and 2.8, decreasing computational time significantly. This simplified description reproduces trends in the statistically steady-state disloca-

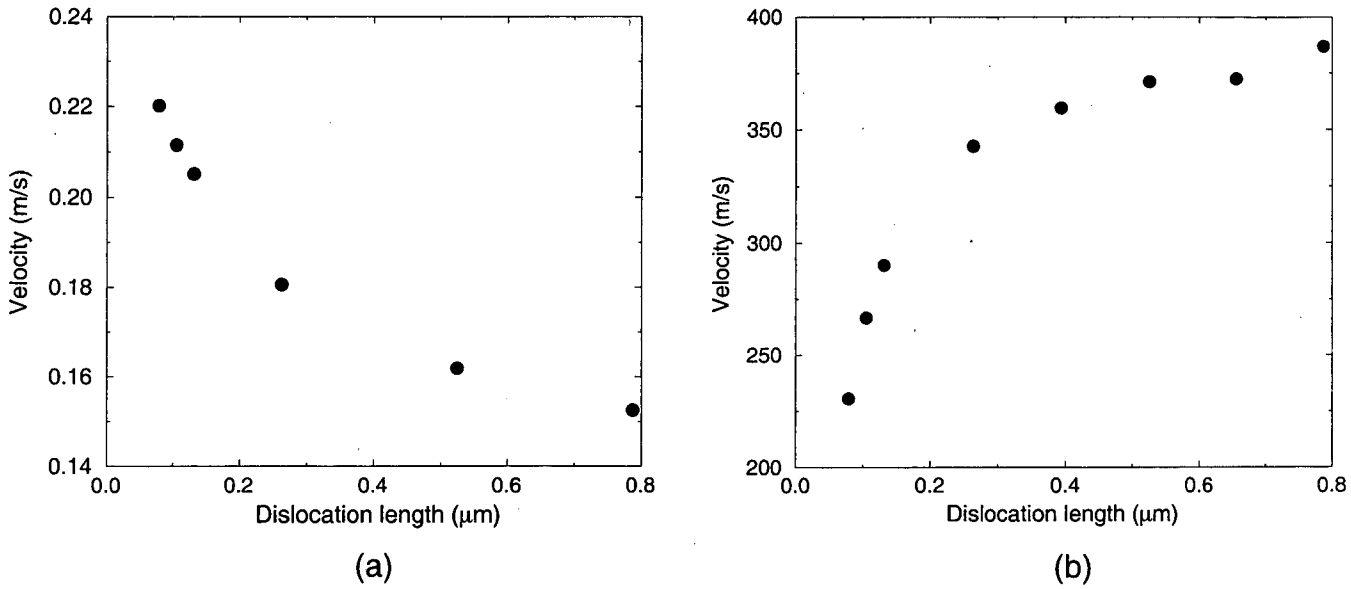

Figure 2.5: Dislocation velocity vs. length for an applied stress of (a) 100 MPa and (b) 400 MPa at a sample temperature of 450 K.

tion velocities calculated from the full simulation while allowing the examination of longer dislocation lengths. (The simple model does not, however, accurately reproduce the small-scale structure of the dislocation, and thus is used only for the purpose of examining dislocation velocity.)

Dislocation velocity is determined within the model as follows. The mean dislocation position $\bar{y}$ at a given time t is computed by performing an average over the positions of the screw segments, weighted by their lengths. In the steady state, the dislocation velocity $v = \langle d\bar{y}/dt \rangle$ will become a constant (in a statistical sense) which can be found by fitting a line to a plot of $\bar{y}$ vs. t.

Figure 2.5 shows the steady state dislocation velocity as a function of dislocation length under applied stresses of 100 MPa and 400 MPa, at a temperature of 450 K. It should be noted that the absolute values of the velocities depend on the choice of the attempt frequency ω_o and are not meant to be compared to experimental values; rather, they are shown to illustrate qualitatively the different regimes of length dependence.

The dependence of the dislocation velocity on length is a result of two differ-

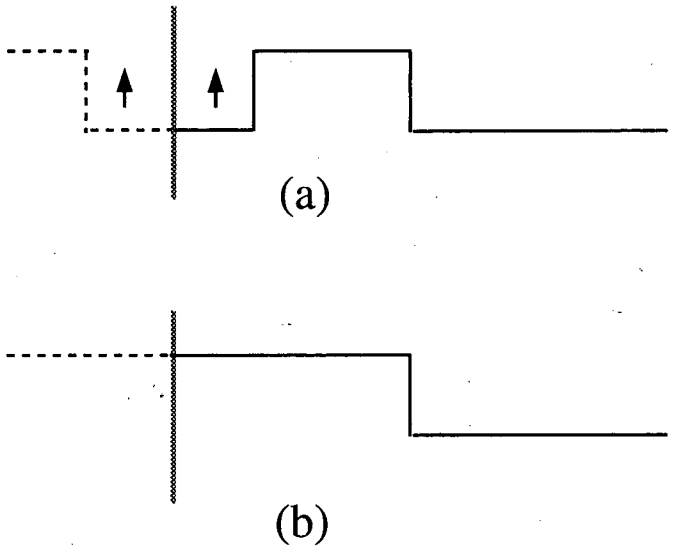

Figure 2.6: At low stresses, kink pairs tend to "stick" only when nucleated near a surface. (a) Single kink annihilates with its image. (b) Mobile kink remains in bulk, free to move.

ent surface effects, and the nature of the dependence (*i.e.* whether velocity increases or decreases with length) is determined by the dominance of one effect over the other in different regions of parameter space. On one hand, surfaces can be thought of as kink sources, for they serve to enhance the velocity in the following manner: A kink pair is most likely to "stick" when it is nucleated close to the surface, after which the adjacent single-kink annihilation (with its image) is energetically favored, leaving the remaining kink to move laterally within the dislocation. (See Figure 2.6.) Thus, nucleation of a kink pair near a surface is favored over nucleation in the bulk. On the other hand, surfaces also decrease the velocity in that the finite size of the dislocation places a limit on the number of kink pairs that can be present [6]. In this manner, free surfaces can also be thought of as kink sinks.

At low stresses, kink pairs are very unstable and the source behavior of the surface dominates. The dislocation velocity is closely related to the probability of nucleating a kink pair near the surface, since kink pairs nucleated in the bulk are likely to annihilate in the next kinetic Monte Carlo step. This probability is determined

by the ratio of surface nucleation sites to bulk nucleation sites. The ratio decreases as the dislocation length is increased, leading to an overall decrease in dislocation velocity as a function of length.

At high stresses, nucleated kink pairs both at the surface and in the bulk are quite stable. Although nucleation at the surface is still favored, there are many more sites in the bulk, and all kink pairs tend to "stick". Once the kinks are nucleated, they spread along the dislocation under the influence of the applied stress until they reach the surfaces. The sink behavior of the surface now dominates; the length dependence of the velocity here is now a consequence of the finite size of the dislocation. If the dislocation is shorter than the equilibrium kink separation, very few (typically, only one) kink pairs can be present at a time before the kinks move off the surface. As the dislocation length increases, more opportunities for kink pair nucleation arise and the dislocation can thus advance more rapidly.

This tendency of the free surfaces to act as kink sources at low stresses and as kink sinks at high stresses can be modeled by the following equation for slip per unit length:

$$\frac{\partial y}{\partial t} = D\frac{\partial^2 y}{\partial x^2} + \alpha \sum_{n=-\infty}^{\infty} \delta(x - nL) + \beta. \tag{2.16}$$

Here y represents the slip per unit length of the dislocation, D is a kink diffusion coefficient, and L is the dislocation length. β is related to the nucleation rates in an infinite dislocation, and α is related to an *additional* contribution to the nucleation rates at the surfaces. It is expected that $\alpha > 0$ for low stresses (nucleation rates are higher at the surfaces) and $\alpha < 0$ for high stresses (nucleation rates are lower at the surfaces). The sum is taken to be infinite in order to facilitate solution, with the understanding that only the range $0 < x < L$ is relevant to the problem at hand.

Solving Eq. 2.16 for y (see Appendix A) yields

$$y(x,t) = \left(\frac{\alpha}{L} + \beta\right) t + \frac{\alpha L}{2\pi^2 D} \sum_{m=1}^{\infty} \frac{cos(2\pi m x/L)(1 - e^{-4D\pi^2 m^2 t/L^2})}{m^2}. \tag{2.17}$$

The dislocation motion is thus described by a constant velocity term and a term that modifies the shape of the dislocation, causing it to form a bowed structure. The strength of this "bowing" depends on both the dislocation length and on α,

the additional contribution to dislocation slip at the surface. When $t \to \infty$, the time-dependent contribution of this bowing term disappears and the steady-state dislocation velocity is simply

$$\frac{\partial y}{\partial t} = \frac{\alpha}{L} + \beta \tag{2.18}$$

where β now gives the dislocation velocity in the limit of infinite length and α determines the strength of the length dependence. Using Eq. 2.18, one can fit velocity vs. length curves (such as those in Fig. 2.5) to determine α and β as a function of stress and temperature. A contour plot of α/β, where $L^* = |\alpha/\beta|$ is the characteristic length below which finite-size effects may be significant, is shown in Fig. 2.7. As expected, α is found to be negative for high stresses and positive for low stresses. The line along which $L^* = 0$ marks the set of stress-temperature pairs where velocity is effectively independent of dislocation length. However, the values of L^* reported here for other stresses and temperature are short, approximately 400 Å. The velocity of dislocations substantially longer than this will be unaffected by finite size.

2.2.2 Stress and temperature dependence

Using the full simulation with the complete elastic calculation, the dependence of the steady state velocity of the dislocation on applied stress and sample temperature can now be studied in detail. Figure 2.8 displays the dislocation velocities as a function of applied stress at temperatures of 300, 450, and 600 K, using dislocation lengths of $2000b$ ($\approx$ 5200 Å). For $T = 450$ K and $T = 600$ K, this is well beyond the region of strong length dependence and the velocities can be considered to be the same as those in the infinite-length limit. For $T = 300$ K, this dislocation length is still in the regime where there is significant length dependence. As can be seen from examination of Figure 2.7, the characteristic length L^* is somewhat higher for $T = 300$ K in the stresses of interest. Moreover, α is negative in this region, suggesting that the velocities observed are slightly lower than those in the infinite-length limit.

In fact, this suggestion is confirmed by close examination of Fig. 2.8, which reveals that the $T = 300$ K curve crosses the other two curves at a higher stress than

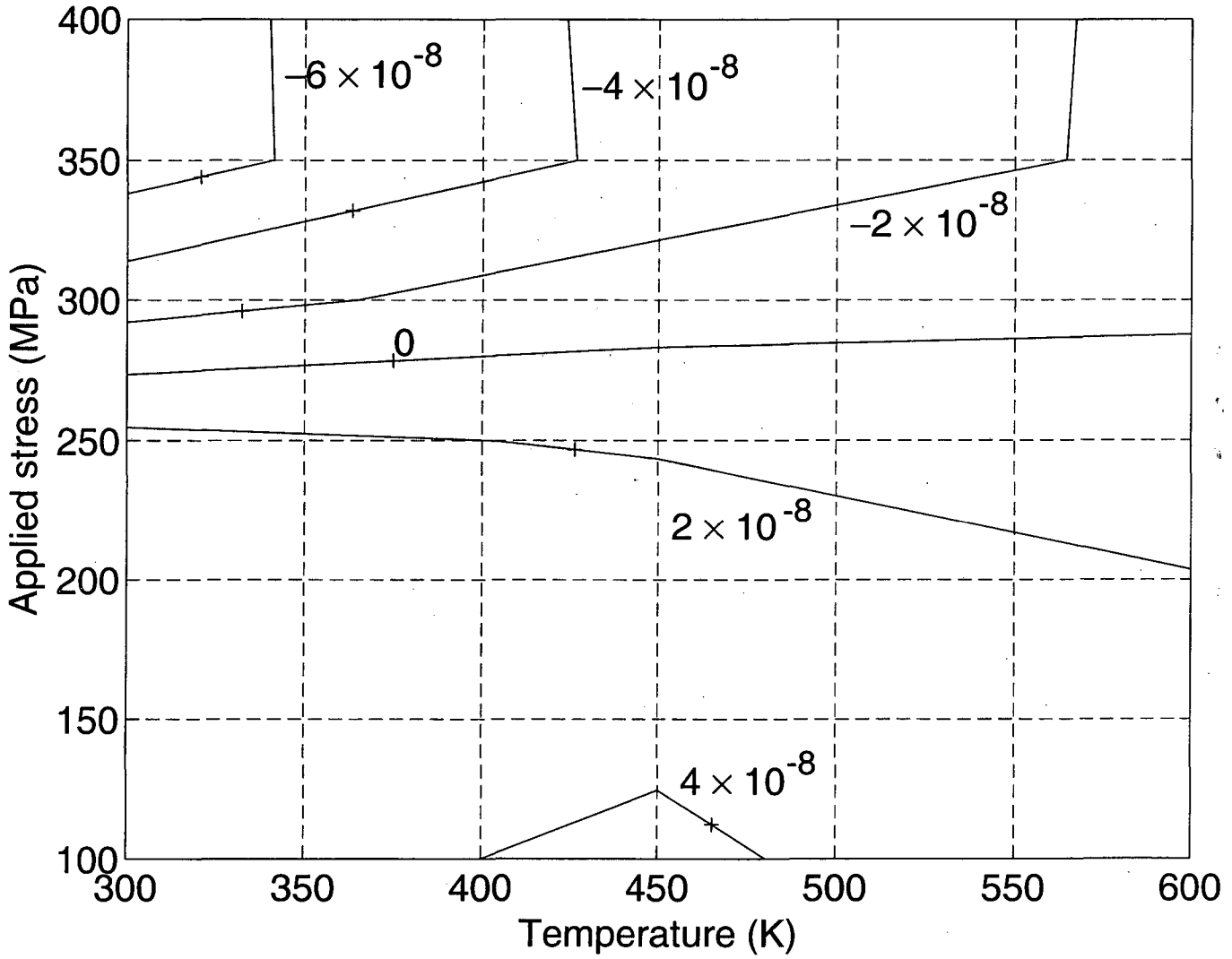

Figure 2.7: Contour plot of the characteristic dislocation length α/β, in meters, as a function of applied stress and temperature. The line marked 0 indicates the set of parameters where velocity is independent of dislocation length.

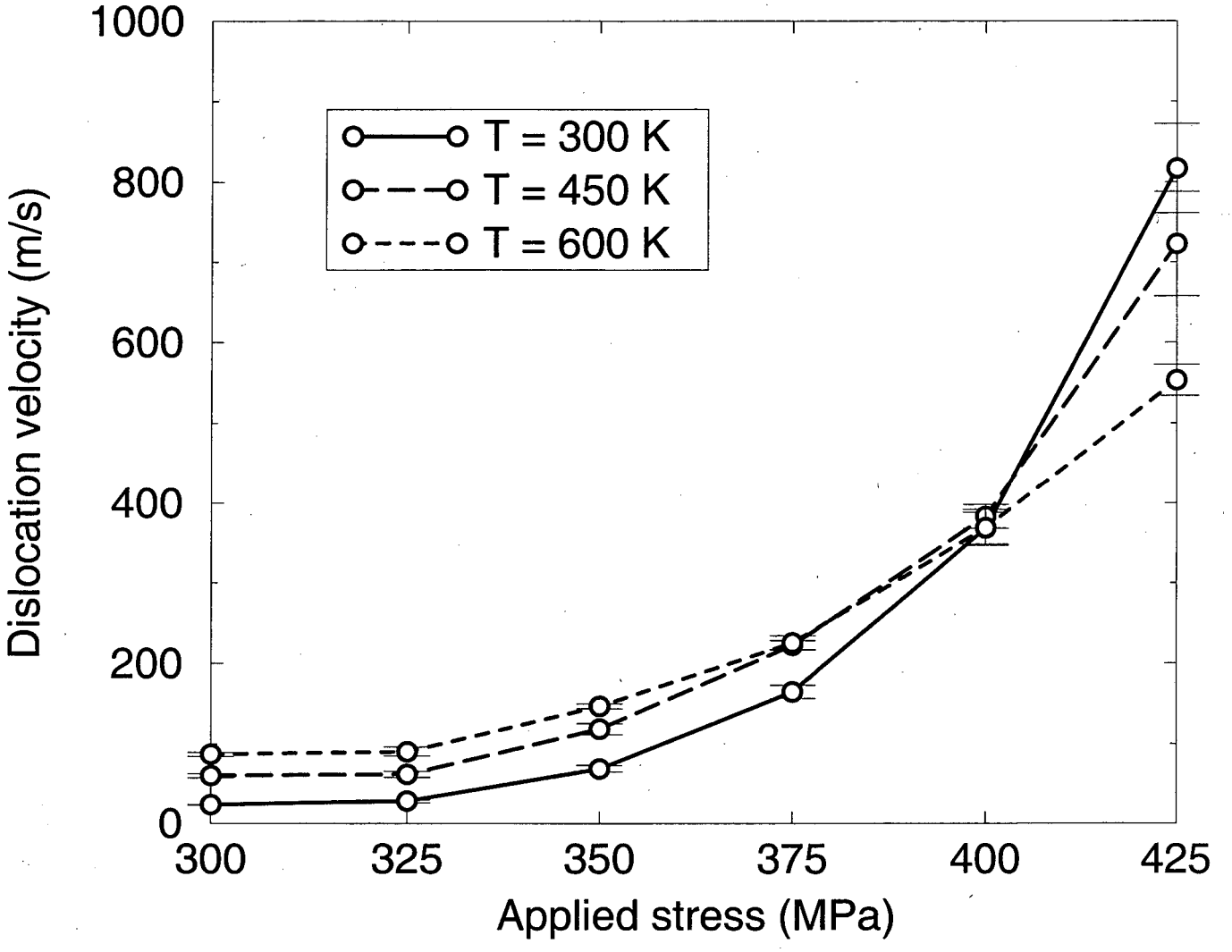

Figure 2.8: Steady-state dislocation velocity as a function of applied stress for T = 300, 450, and 600 K.

they cross each other. Although it is impractical to generate the entire $T = 300$ K curve with a sufficiently long dislocation due to the computational time needed for such a calculation, it is found by calculating the velocities at the two points $\sigma = 375$ MPa and $\sigma = 400$ MPa for a long dislocation that the $T = 300$ K curve will indeed cross the others at the same point in the infinite-length limit. The stress at which this point occurs, ≈ 385 MPa, corresponds to the zero-temperature yield stress for a dislocation of infinite length, as is now discussed.

The crossing of the curves at high stress can be understood as follows. The six processes that govern the motion of the dislocation are kink pair nucleation with (*i.e.* in the direction favored by) or against an applied stress, kink pair annihilation with or against the stress, and lateral kink motion with or against the stress. One may suppose that the velocity of the dislocation is primarily determined by the complementary processes of kink pair nucleation with the stress and kink pair annihilation against the stress. This is not an unreasonable assumption, since kink pair nucleation against the stress occurs rarely and lateral kink motion can occur only after kinks have been nucleated. To explore the relative importance of these two primary processes, the energy barrier associated with each process was plotted as a function of stress, assuming an isolated kink pair in the middle of an otherwise flat dislocation. Since the energy barrier for kink pair nucleation with the stress decreases with increasing stress and the energy barrier for kink pair annihilation against the stress increases with increasing stress, the curves must eventually cross, and do so around 410 MPa. (This does not correspond exactly to the crossing point $\sigma_c \approx 385$ MPa observed in Figure 2.8, since this simple analysis does not take into account the influence of the configuration-dependent long-ranged elastic fields as well as the other processes that affect the motion of the dislocation.) The ratio of the two rates, assumed to be related to the velocity, is given by

$$R_{nuc}/R_{ann} = \exp(-\Delta E/kT) \tag{2.19}$$

with ΔE given by

$$\Delta E = E_{nuc} - E_{ann} \tag{2.20}$$

where E_{nuc} and E_{ann} are the energy barriers associated with kink pair nucleation and annihilation, respectively. At low stresses $\sigma < \sigma_c$, $E_{nuc} > E_{ann}$ and ΔE is positive; as T increases, the ratio of the rates (and thus the dislocation velocity) also increases. This produces the expected behavior. However, at high stresses $\sigma > \sigma_c$, $E_{nuc} < E_{ann}$ and ΔE is negative, indicating that it is actually energetically favorable to nucleate double kinks. Therefore, as T increases, the exponent goes from a positive number toward zero and the velocity actually decreases.

This phenomenon can be understood as the result of the competing effects of temperature and applied stress. Thermal effects alone do not give a directional preference for the motion of the dislocation, and the kinks are as likely to nucleate "backward" ($-y$ direction) as "forward" ($+y$ direction). At high stresses, the dislocation motion in the forward direction is so energetically favored that it needs no help from thermal effects in order to overcome the elastic and Peierls barriers to motion. A higher temperature increases the likelihood of kink nucleation and motion in both directions. This has little effect on the "forward-moving" events of the dislocation, since those would occur anyway, but the frequency of "backward-moving" events is increased. Thus, the motion of the dislocation is actually hampered at high stresses by thermal effects.

In the limit of an infinitely long dislocation, then, velocity vs. stress curves at different temperatures are expected to cross at the same stress $\sigma_c \approx 385$ MPa. As temperature is decreased, the curves should become steeper (see Figure 2.9). Finally, in the limit of zero temperature, the curve is vertical, corresponding to a yield stress at σ_c.

2.3 Dynamic scaling of dislocation width

The discrete nature of the dislocation model suggests an analogy, pictured in Figure 2.10, with the growth of thin films on a one-dimensional substrate [6]. Double-kink nucleation/annihilation corresponds to adatom deposition/evaporation on the flat substrate, and kink motion corresponds to addition/removal of an atom at a ledge. Several models of crystal growth [35, 36] have been well-studied, and a

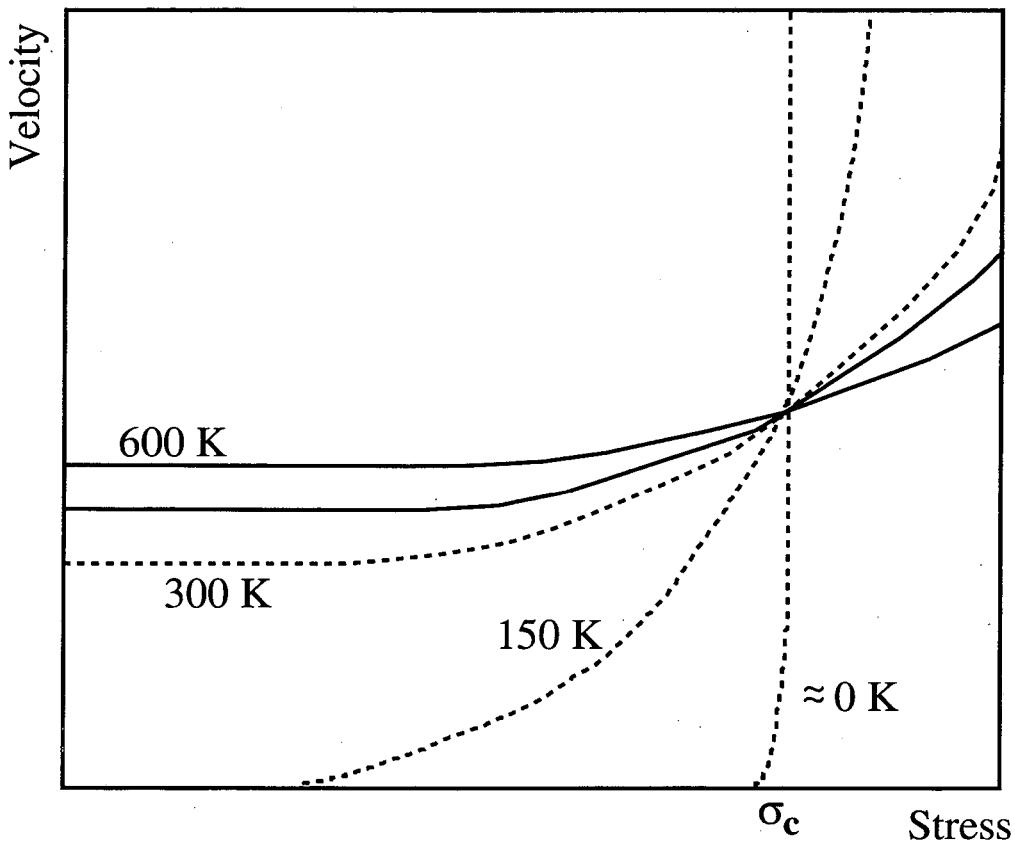

Figure 2.9: Schematic illustration of velocity vs. stress curves for an infinite-length dislocation as the temperature approaches zero. Solid lines indicate calculated velocities plotted in Fig. 2.8; dashed lines show the expected behavior as the temperature is decreased. In the limit $T \to 0$, the yield stress is simply σ_c.

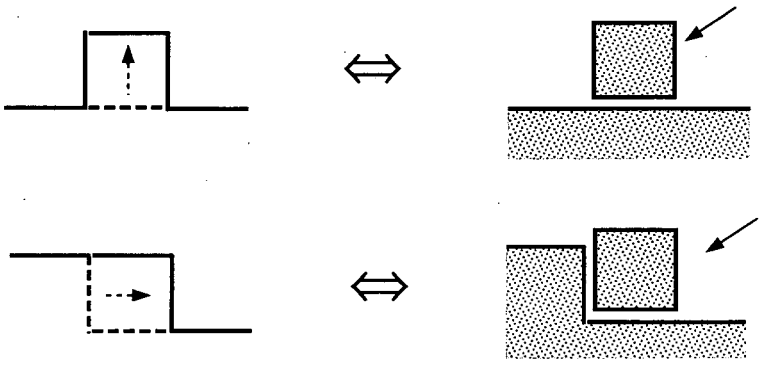

Figure 2.10: Analogy between dislocation motion and thin film growth on a 1-D substrate. Double-kink nucleation/annihilation corresponds to adatom deposition/evaporation on the flat substrate, and lateral kink motion corresponds to addition or removal of an atom at a ledge.

comparison of the results provides a way of characterizing the dynamics of the moving dislocation.

2.3.1 Observation of kinetic roughening

In crystal growth models, surfaces typically display dynamic scaling behavior. One commonly studied aspect of this behavior is the dynamic scaling of the interface roughness, defined for a d-dimensional system as [37]

$$w(L,t) = \left[L^{-d}\int d^d x\,(h(\mathbf{x},t) - \bar{h}(t))^2\right]^{1/2} \tag{2.21}$$

where L is the linear size of the system, $\mathbf{x}$ is the position on the substrate, $h(\mathbf{x},t)$ is the height of the interface as a function of position and time, and $\bar{h}(t)$ is the spatial average of the height

$$\bar{h}(t) = L^{-d}\int d^d x\, h(\mathbf{x},t). \tag{2.22}$$

The dislocation width in the discrete system can be defined analogously as

$$w(L,t) = L^{-1/2}\left\{\sum_{i=1}^{N}(y_i(t) - \bar{y}(t))^2\right\}^{1/2} \tag{2.23}$$

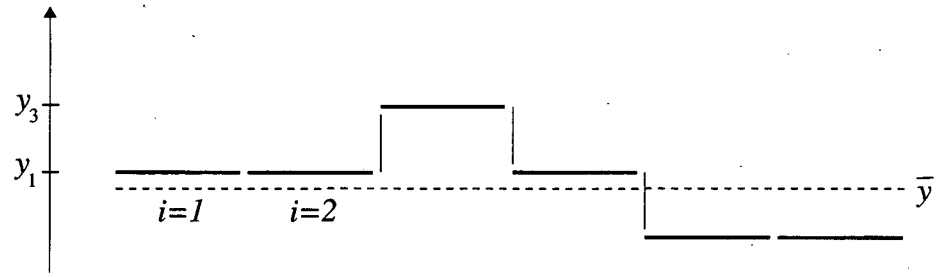

Figure 2.11: Definition of quantities for Eqs. 2.23 and 2.24. The solid line is the dislocation, with screw segments shown thicker.

where N is the number of segments, *i.e.* the length of the dislocation is $L = 20bN$, $y_i(t)$ is the position of screw segment i in the dislocation at time t, and $\bar{y}(t)$ is the average position of the dislocation at time t:

$$\bar{y}(t) = \frac{1}{N}\sum_{i=1}^{N} y_i(t). \tag{2.24}$$

(For the purposes of Eqs. 2.23 and 2.24, a "segment" always has length $20b$ according to the discretization of the lattice. This is in contrast to the rest of the text, where the term refers to an dislocation line of any length that has constant direction and Burgers vector. See Figure 2.11.)

A growth process exhibits dynamic scaling if the configurations can be made equivalent (in a statistical sense) by simulataneously rescaling height, time, and position. The rescaled configurations $\tilde{h}(x,t)$ can be written

$$\tilde{h}(x,t) = a^{-\zeta} h(ax, a^z t) \tag{2.25}$$

where a is an arbitrary positive number and ζ and z are characteristic scaling exponents (called the *roughness* and *dynamic* exponents, respectively). By choosing $a = 1/x$, this can be recast in the form

$$\begin{aligned} h(x,t) &= x^{\zeta} h(1, t/x^z) \\ &= x^{\zeta} f(t/x^z). \end{aligned} \tag{2.26}$$

In the limit $t \to \infty$, $h(x,t) - \bar{h}(t)$ is expected to become stationary, or independent of t. With the initial condition $h(x,0) = 0$, the growth of the system

should be unaffected by position at the early stages; thus $h(x,t) - \bar{h}(t)$ should be independent of x at small times. These two limiting behaviors can be summarized as conditions on the scaling function $f(r)$ [37]:

$$f(r \to \infty) = \text{const} \tag{2.27}$$

$$f(r \to 0) \sim r^{\zeta/z}. \tag{2.28}$$

For systems of finite size, x is replaced by the system size L [36]. Thus, $w(L,t)$ exhibits dynamic scaling if it satisfies the form

$$w(L,t) = L^{\zeta} f(t/L^z). \tag{2.29}$$

If $w(L,t)$ obeys the above scaling law, plots of $L^{-\zeta}w(L,t)$ vs. t/L^z should collapse onto the scaling function $f(r)$. Figure 2.12 shows scaled plots of dislocation width vs. time for four dislocation lengths, averaged over at least 200 trials to reduce the effect of statistical noise. (Unscaled data are shown in the inset.) By eye, best collapse of the data was achieved with the exponents $\zeta = 0.53$ and $z = 1.55$.

It should be noted that this dynamical scaling of the dislocation width can only be observed in the limit in which the bowing of the dislocation predicted by Eq. 2.17 is much less than the width predicted by Eq. 2.23. The bowing predicted from Eq. 2.17 scales with α, and hence the ideal parameters for the study of this behavior are those along the contour $\alpha/\beta = 0$ in Fig. 2.7. In practice, however, producing Fig. 2.7 for the full simulations (including all elastic interactions), and thus determining these parameters accurately, is difficult. However, the stress and temperature parameters (σ = 300 MPa, T = 450 K) used for the simulation data in Figure 2.12 correspond to a low L^* for the simple model, and the observation of scaling suggests that the values of L are well beyond the limit where the bowing is significant.

The exponents ζ and z can be determined exactly for certain continuum models of growth. One such model is the Kardar-Parisi-Zhang (KPZ) equation, which appears in one dimension as [35]

$$\frac{\partial y}{\partial t} = \Lambda \frac{\partial^2 y}{\partial x^2} + \lambda \left| \frac{\partial y}{\partial x} \right|^2 + \eta(x,t) \ . \tag{2.30}$$

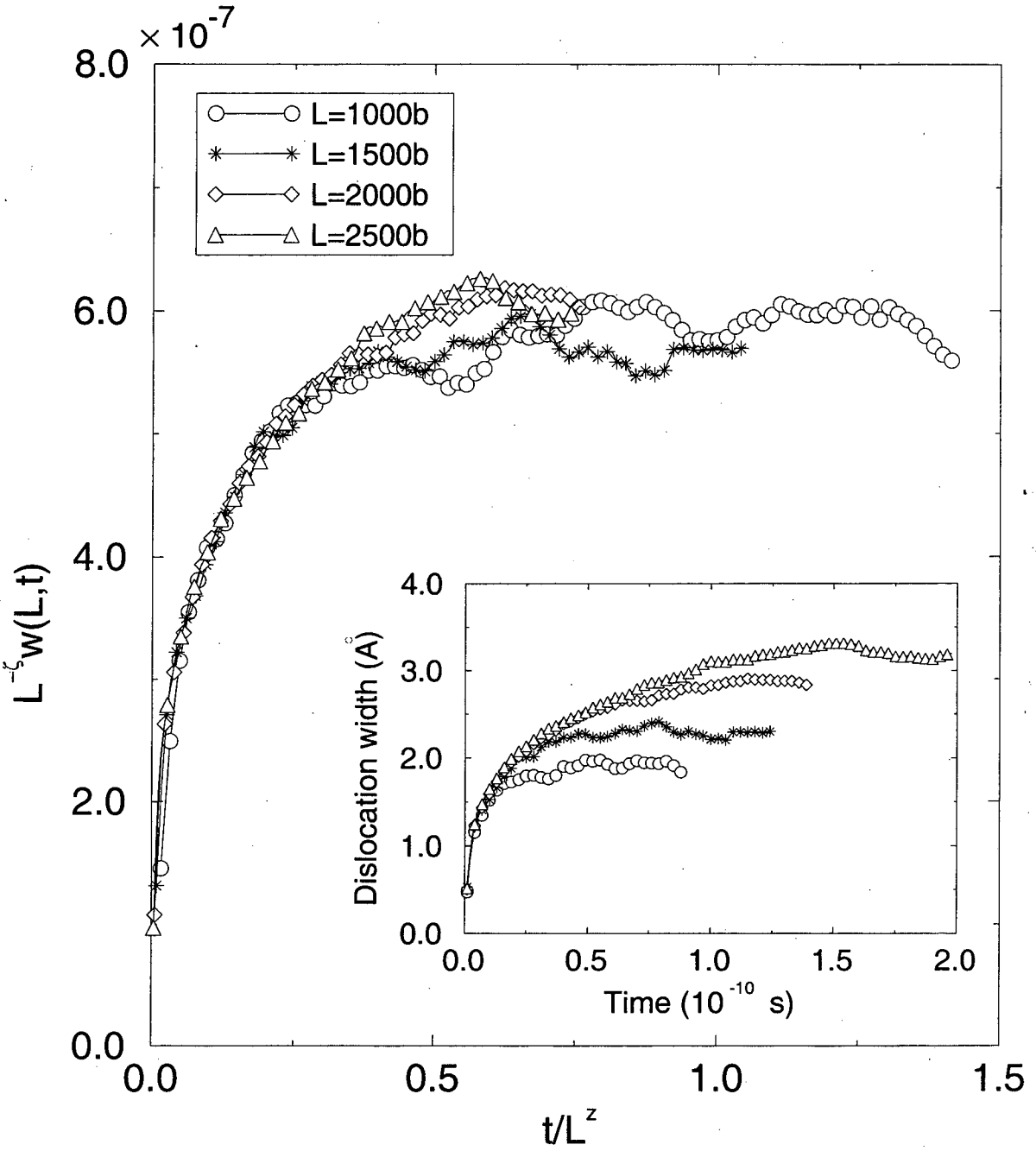

Figure 2.12: Dislocation width vs. time for four dislocation lengths, scaled according to Eq. 2.29 using exponents of $\zeta = 0.53, z = 1.55$ (unscaled data are shown in the inset). Data are for an applied stress of 300 MPa and temperature 450 K.

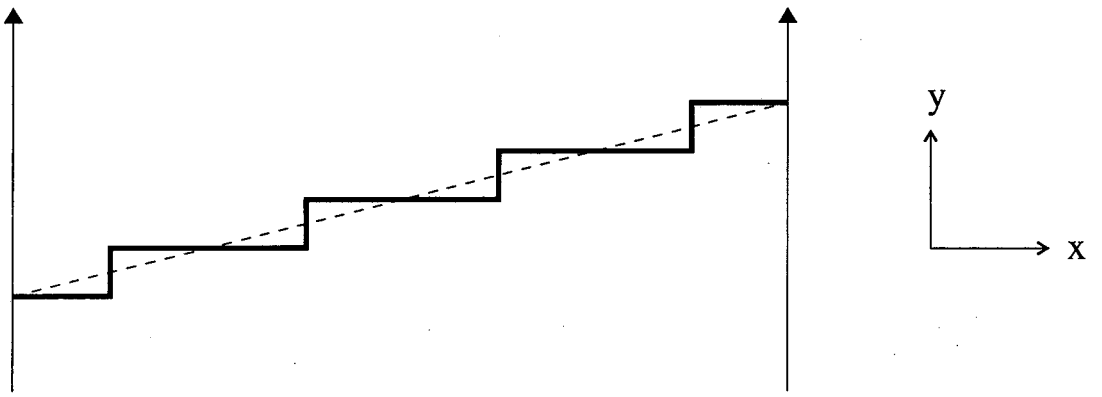

Figure 2.13: Perfectly ordered dislocation configuration. The slope of the dislocation is marked by a dotted line.

Here h is the displacement (in the slip plane) of the dislocation position x, Λ represents the strength of the line tension, and $\eta(x,t)$ is a Gaussian white noise term. For $\lambda \neq 0$, the values $\zeta = 1/2$ and $z = 3/2$ [35, 37] are obtained. For $\lambda = 0$, the KPZ equation reduces to the Edwards-Wilkinson equation, for which $\zeta = 1/2$ and $z = 2$ [38].

2.3.2 Analysis of scaling results

In Eq. 2.30, $\lambda \neq 0$ corresponds to a dependence of the dislocation velocity on the local slope. The proximity of the observed scaling exponents $\zeta = 0.53$ and $z = 1.55$ to the KPZ exponents $\zeta = 1/2$ and $z = 3/2$ suggest that the dislocation velocity does have this slope dependence. In order to see whether this dependence can be observed, the expectation value of the dislocation velocity can be calculated for perfectly ordered configurations, *i.e.* configurations for which the slope is constant throughout the dislocation, within the limits imposed by the discrete lattice. (See Figure 2.13.)

The expectation value for the dislocation velocity for a particular configuration is

$$\langle v \rangle = \sum_{i=1}^{N} P_i \, v_i \tag{2.31}$$

where N is the total number of possible events (kink pair nucleation, kink pair anni-

hilation, lateral kink motion), P_i is the probability that event i will occur in the next kinetic Monte Carlo step, and v_i is the dislocation velocity associated with event i. If

$$R = \sum_{i=1}^{N} R_i \tag{2.32}$$

is the sum of the individual rates, then

$$P_i = \frac{R_i}{R} \tag{2.33}$$

and

$$v_i = R\,(\Delta\bar{y})_i \tag{2.34}$$

where $(\Delta\bar{y})_i$ is the change in the average position of the dislocation $\bar{y}$ if event i occurs. Thus, Eq. 2.31 becomes

$$\langle v \rangle = \sum_{i=1}^{N} R_i (\Delta\bar{y})_i. \tag{2.35}$$

Using the above scheme, v is plotted as a function of the dislocation slope dy/dx in Figure 2.14. The slope dependence is apparent, and is consistent with the observation of KPZ scaling. With perfectly ordered configurations, this dependence of the velocity on the slope of the dislocation can easily be seen to arise from the difference between the rates of double-kink nucleation and lateral kink motion. For a perfectly flat dislocation, no kinks are present and the expectation value of the velocity thus depends only on the rate of kink pair formation. For a maximally sloped dislocation, there exist no sites for kink pair formation and the velocity depends only on the rate of lateral kink motion. A dislocation with an intermediate slope will have its velocity determined by both rates, weighted according to the number of sites for each type of event. Since rates for double-kink nucleation and lateral kink motion are expected to be different in general, one expects always to observe KPZ scaling of the dislocation width within this model, regardless of the choice of parameters.

The sharp decrease in v for the outermost points (corresponding to the maximum value of $|dy/dx|$) is a consequence of the solid-on-solid condition imposed on the model when the maximum number of kinks is present (as illustrated in Figure 2.13). Since kinks in the bulk cannot move under these conditions (for the model does

not allow same-signed kinks of length a to coalesce into a single kink of length $2a$), the dislocation motion is restricted to the activity of single kinks at the surface, and only two events are possible. The solid-on-solid condition, which prevents the creation of these extended edge segments as well as "overhangs", is likely to be exerting a smoothing effect on the dislocation, thus restricting its width. If so, then the kinetic roughening observed here represents a lower bound on the effects of the nonlinearity; in any case, it is clear that these nonlinearities cannot be neglected in considering the dynamics of the dislocation.

2.4 Conclusions

This study of a single dislocation moving in a Peierls potential has enabled a closer look at the parameters and processes most significant to the simulation of dislocation dynamics. It is found that free surfaces may either aid or hinder the motion of the dislocation, depending on the magnitude of the applied stress and sample temperature. The velocity of the dislocation is observed to decrease with length for low stresses and increase with length for high stresses. A continuum model for the velocity and shape of the dislocation is developed which takes into account the tendency for the free surfaces to act both as kink sources and as kink sinks.

The dislocation velocity is also studied as a function of applied stress for different temperatures. At low stresses, thermal fluctuations enhance the mobility of the dislocation, and the velocity of the dislocation increases with increasing temperature. At high stresses, the nucleation of double kinks is favored, and thermal fluctuations serve to decrease the double kink nucleation rate, hence slowing the dislocation. It is argued that the stress at which the velocity is temperature independent, for a dislocation of infinite length, corresponds to the zero-temperature yield stress.

Through an analogy with models of thin film growth, the dislocation width is seen to exhibit dynamic scaling governed by exponents predicted by the Kardar-Parisi-Zhang equation. This result corresponds to a dependence of the dislocation velocity on the local slope of the dislocation. This dependence can be explicitly observed, and arises from the difference in the rates of the two possible types of

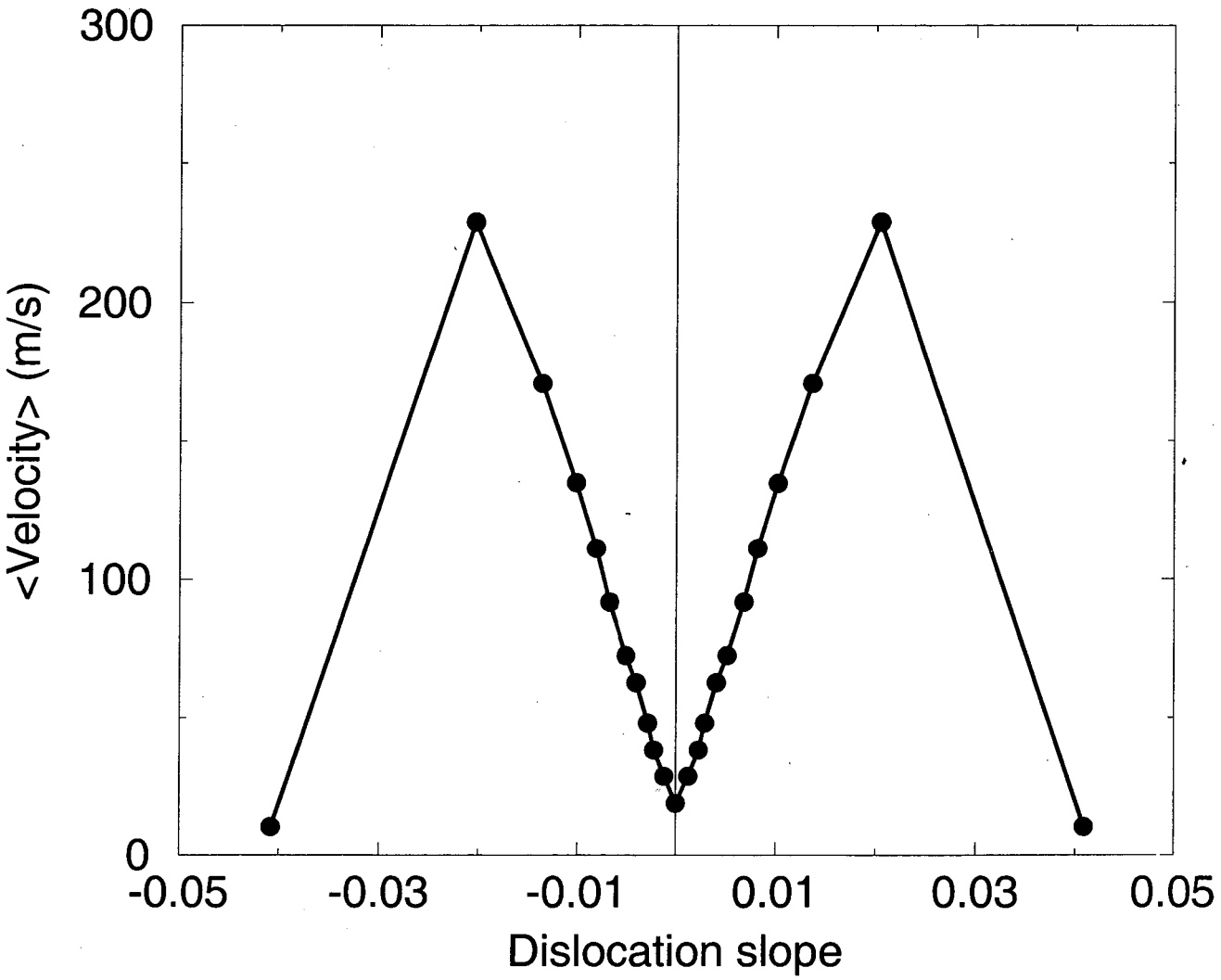

Figure 2.14: Expectation value of the dislocation velocity for a perfectly ordered sloped dislocation as a function of the slope, for $L = 2000b$, $\sigma = 300$ MPa, and T = 450 K. This dependence suggests that the λ of Eq. 2.30 is nonzero, consistent with the values observed for the scaling exponents ζ and z.

events, kink-pair formation/annihilation and lateral motion of a single kink. Since these rates are expected to be different in general, the model suggests that KPZ scaling will be observed for dislocations under applied stresses and temperatures in which finite-size effects are insignificant.

Although much qualitative information has been gleaned from this simple simulation, it remains clear that a good *quantitative* understanding of the dynamics requires better values for the basic parameters entering the model, such as the Peierls stress and the core radius (which is related to the interaction cutoff parameter ρ). As these numbers are ultimately related to the atomic scale structure and response to stress of the dislocation core, it is valuable to study the dislocation core in greater detail, in hopes that one may extract parameters useful for these larger scale simulations. This is the motivation for the work described in Chapters 3 and 4.

Chapter 3

The 90° partial dislocation core in diamond†

Although elasticity theory suffices for many aspects of the study of dislocations, in order to understand fully the properties of dislocations at small distances, one must consider the structure of the dislocation on an atomic scale. Currently, computational techniques have advanced to the point that it is possible to study the energetics of hundreds of atoms using very accurate electronic structure calculations. By performing these techniques on systems large enough that the dislocation core structure and dislocation interactions can be studied, it is hoped that one will be able to extract parameters for elasticity theory to increase the accuracy of larger-scale simulations.

The work presented in this chapter focuses on the core structure and energy of the 90° partial dislocation in diamond, using a combination of *ab initio* calculations and isotropic elasticity theory. The method of periodic supercells is introduced and employed, and the relative energies of two possible core reconstructions are examined. By considering an infinite array of dislocation dipoles as a one-dimensional stack of tilt boundaries, values for the shear modulus μ and core radius r_0 are extracted, and found to agree well with experimental values and theoretical estimates.

†The research presented in this chapter has been submitted for publication (Ref. [39]).

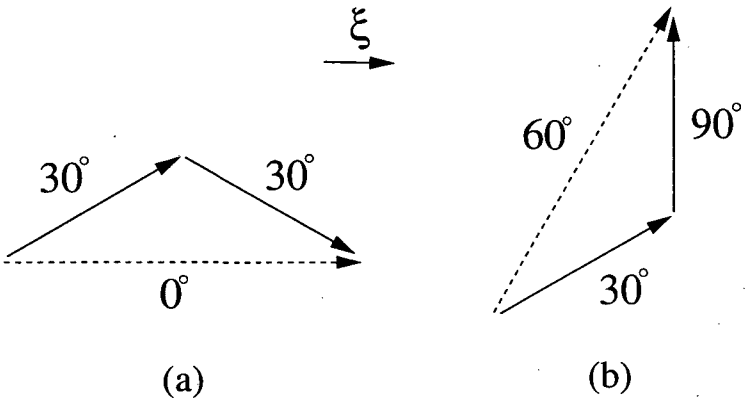

Figure 3.1: Dissociation of (a) a 0° dislocation into two 30° partials and (b) a 60° dislocation into a 30° and a 90° partial. Arrows and labels indicate the direction of the Burgers vector and the angle made with the line direction.

3.1 Introduction to the 90° partial

3.1.1 Slip system of diamond cubic crystals

Since the diamond cubic lattice is based on the fcc lattice, dislocations lie in the close-packed $\{111\}$ planes in the $\langle 110 \rangle$ directions with Burgers vectors of type $\frac{1}{2}\langle 110 \rangle$. By convention, dislocations in these crystals are identified by the angle made by the Burgers vector $\mathbf{b}$ and the line direction $\boldsymbol{\xi}$. Thus, the predominant dislocations are the 0° and 60°. As discussed in Section 1.2.7, it is energetically favorable for such dislocations to dissociate into partial dislocations separated by a ribbon of stacking fault. As Figure 3.1 shows, the 0° dislocation splits into two 30° partials, whereas the 60° splits into a 30° and a 90° partial.

3.1.2 Reconstructions of the 90° partial dislocation

The unreconstructed core of the 90° partial dislocation in a diamond cubic material contains a zigzag chain of three-fold coordinated atoms (Figure 3.2(a)). In 1979, it was proposed by Hirsch [40] and Jones [41] that this core reconstructs by breaking the mirror symmetry along the dislocation line, restoring the fourfold co-

ordination of the atoms in the core; in accordance with the literature, this will be referred to as the single-period, or SP, structure (Figure 3.2(b)). Recently, however, Bennetto *et al.* [42] proposed a new structure (hereinafter referred to as the double-period or DP structure) which also restores fourfold coordination to the core atoms, but doubles the periodicity along the dislocation line by creating alternating five- and seven-membered rings (Figure 3.2(c)). Using periodic boundary conditions and a variety of energy calculation methods, the authors showed that the DP structure has a lower energy than the previously assumed SP structure. Although this structure was originally proposed for the 90° partial in silicon, it was later found by the authors [43], again within the periodic supercell framework, that the DP structure is more stable for diamond and germanium as well.

3.2 Core energy calculations

3.2.1 Boundary conditions

The choice of boundary conditions can have a significant effect on the observed results, and controversy remains as to the best methods for studying dislocation core structures. Two common approaches for boundary conditions are the "cluster" method and the method of periodic supercells. In the cluster method, a typical practice is to generate initial positions of the atoms in a cylindrical cell surrounding the dislocation core within anisotropic elasticity theory, fix the positions of the atoms on the surface of the cylinder, and allow the remaining atoms to relax. While the cluster method is useful in that it allows the consideration of an isolated dislocation, it suffers from a sensitivity to the initial placement of the dislocation core (discussed more thoroughly in Chapter 4) and treatment of the atoms at the surface.

Periodic boundary conditions eliminate the difficulty of treating the surface atoms present in the cluster method, but introduce an infinite number of interactions between dislocations. When the supercell is small and the dislocations are thus very close together, extreme stress states may result. Moreover, each supercell must have a net zero Burgers vector to avoid a divergence in the elastic strain energy. These

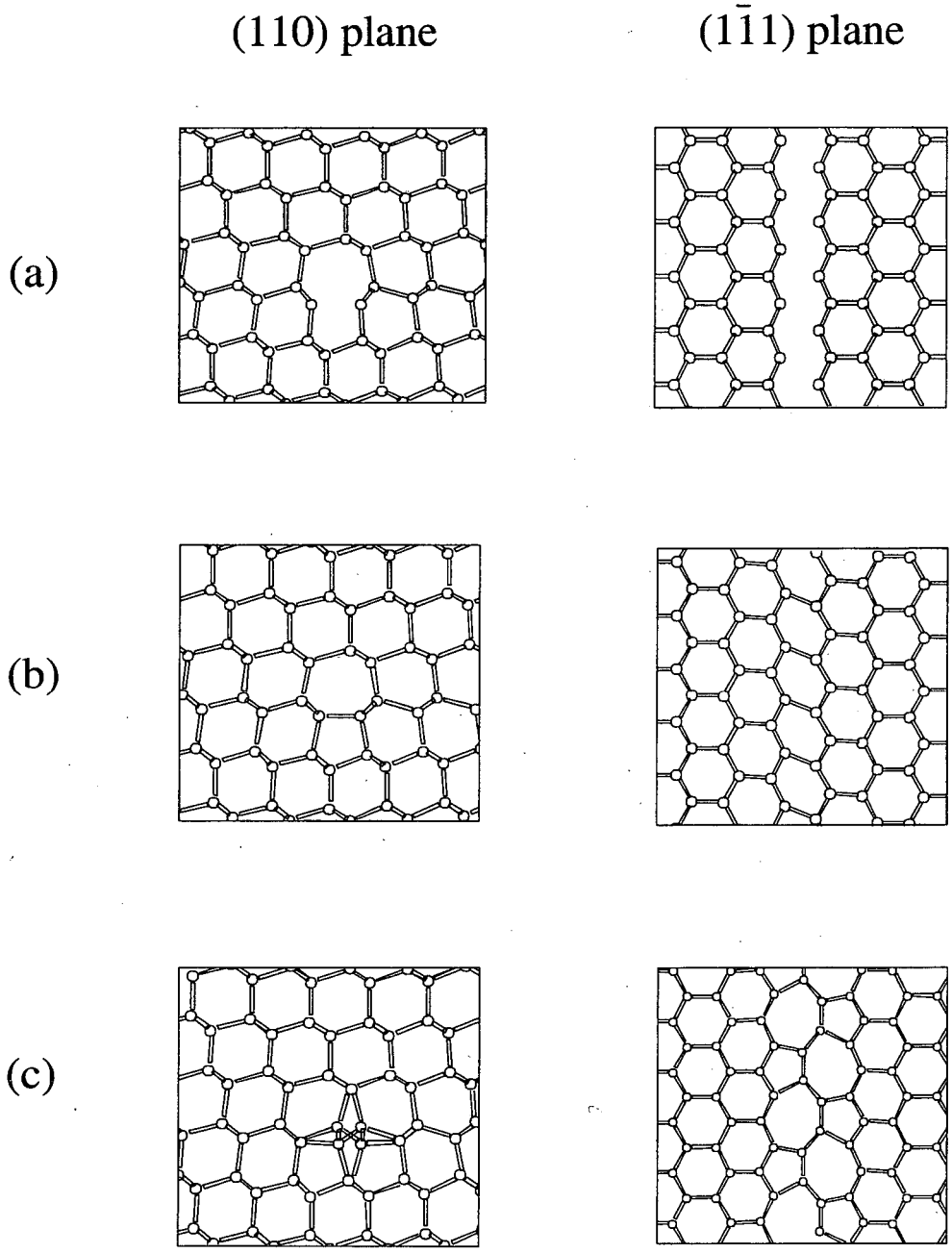

Figure 3.2: Atomic structure of the 90° partial dislocation viewed from above the (110) and (1$\bar{1}$1) planes: (a) unreconstructed, (b) single-period (SP) reconstructed, (c) double-period (DP) reconstructed. Shaded area indicates stacking fault.

difficulties notwithstanding, the periodic supercell method has been the more popular for studies of the core structure and energy of the 90° partial in diamond cubic materials [42, 43, 44, 45, 46] and is the method of choice for the work described in this chapter.

3.2.2 Definition of parameters

The simplest possible cell is a dipolar cell, containing two dislocations with opposite Burgers vector. The dimensions of the cell are defined by the unit vectors in the $(1\bar{1}1)$ plane of the perfect 12-atom orthorhombic cell: $\mathbf{a_1} = \frac{a}{2}[1\bar{1}\bar{2}]$, $\mathbf{a_2} = \frac{a}{2}[110]$, $\mathbf{a_3} = a[1\bar{1}1]$, where a is the lattice constant for diamond, 3.57 Å. (See Figure 3.3). The Burgers vector $\mathbf{b}$ is either $\frac{a}{6}[1\bar{1}\bar{2}]$ or $\frac{a}{6}[\bar{1}12]$, and both dislocations have line direction $\boldsymbol{\xi} = [110]$. The cell has length L and height D, the distance between the dislocations is w, and the offset for adjoining cells is T. (See Figure 3.4). For simplicity, all parameters are expressed as integers, with L, w, and T understood to be in units of $|\mathbf{a_1}|$ and D in units of $|\mathbf{a_3}|$.

Part of the controversy surrounding the discussion of periodic boundary conditions involves the choice of the parameters L, D, w, and T. As first noted by Bigger *et al.* [47], the value of the offset T requires some consideration in order to avoid a lattice mismatch at the cell boundaries. Previously, it was thought that this problem could be solved only by using a "quadrupolar" lattice, *i.e.* $T = L/2$, and several studies [42, 43, 46] have thus employed the quadrupolar lattice exclusively. However, Lehto and Öberg [45] pointed out that this restriction is unnecessary. When two oppositely signed dislocations are introduced into a perfect solid and separated by a distance w, the top and bottom surfaces of the solid are displaced relative to each other by $b(w/L)$, where L is the width of the solid along the slip direction and b is the magnitude of the Burgers vector [9]. Provided that the offset T is adjusted by this amount, there are no restrictions (other than those imposed by the lattice periodicity itself) on L, D, w, and T. Moreover, changing the values of these parameters affects the stresses and stress gradients experienced by a dislocation in the infinite lattice, and the energies observed are expected to depend on these stress states [45].

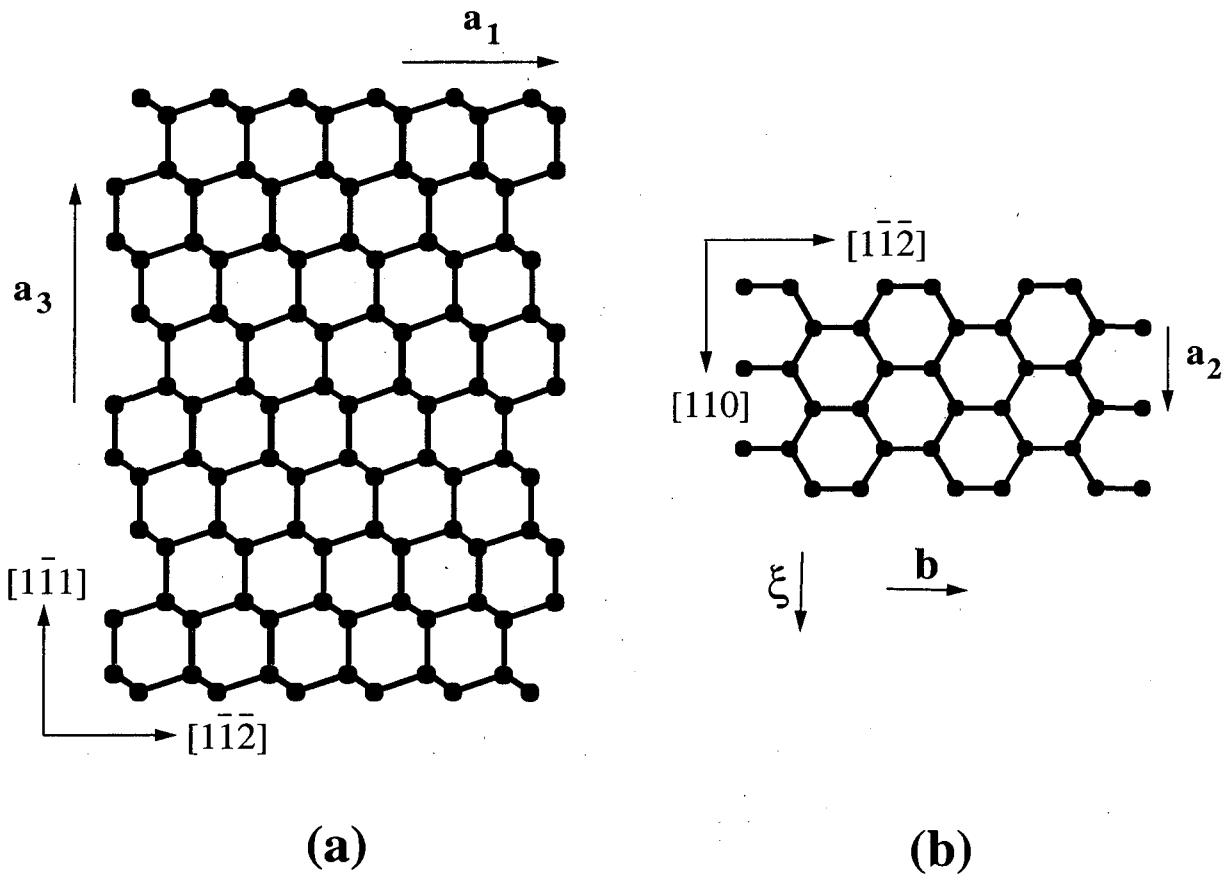

Figure 3.3: Definitions of the unit vectors $\mathbf{a_1}$, $\mathbf{a_2}$, and $\mathbf{a_3}$ in (a) the (110) plane and (b) the (1$\bar{1}$1) plane.

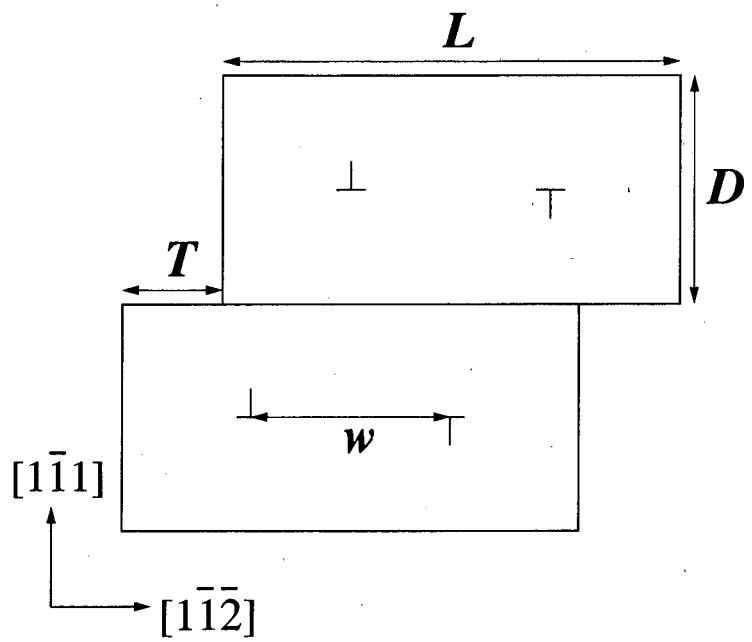

Figure 3.4: Representation of two unit cells in the (110) plane. L is the width of the unit cell, D is the height, and w is the distance between dislocations in the cell. The offset T is also shown.

For the SP reconstruction, there are two possibilities for the dipolar unit cell depending on whether the direction of mirror symmetry breaking is the same (Figure 3.5(a)) or the opposite (Figure 3.5(b)) for the two dislocations. Previous workers [42, 43, 46] have quoted the average of the two distinctly different energies. However, the same sense reconstruction should always be higher in energy. In general, the two regions on either side of the stacking fault are shifted with respect to each other by an arbitrary distance (Figure 3.6(a)). This causes a problem of lattice mismatch at the boundaries which will lead to spurious strains in the system, increasing the energy. In order to avoid this problem, the bonds in the dislocation cores must be angled such that the two regions are shifted with respect to each other by an amount commensurable with the lattice spacing $|\mathbf{a_2}|$ in the dislocation line direction (Figure 3.6(b)). However, this places an artificial constraint on the cell, again increasing the energy. Because the opposite-sense reconstruction does not cause a relative shift of the two regions (Figure 3.6(c)), it is concluded that the opposite sense reconstruction gives the better estimate of the SP core energy, and all calculations considered here are performed with this configuration.

3.2.3 Stress state and energy of a periodic dislocation array

In order to explore how the relative energies of the SP and DP reconstructions depend on stress, it is necessary to sum the stress fields from an infinite number of dislocations. Since the stress field of a dislocation is proportional to $1/r$, where r is the distance from the dislocation, this sum is similar to a Madelung sum for an ionic crystal and must be handled carefully. The sum can be found to converge rapidly when the periodic arrangement of dislocations is viewed as a 1-D stack of tilt boundaries, or linear arrays of dislocations. (See Figure 3.7.)

For a tilt boundary composed of edge dislocations in the coordinate system of Figure 3.8, the stress fields are found by using Eqs. 1.8 to be [6]

$$\begin{aligned}
\sigma_{xy} &= \sigma_0 2\pi X(\cosh 2\pi X \cos 2\pi Y - 1) \\
\sigma_{xx} &= -\sigma_0 \sin 2\pi Y(\cosh 2\pi X - \cos 2\pi Y + 2\pi X \sinh 2\pi X) \\
\sigma_{yy} &= -\sigma_0 \sin 2\pi Y(\cosh 2\pi X - \cos 2\pi Y - 2\pi X \sinh 2\pi X)
\end{aligned} \tag{3.1}$$

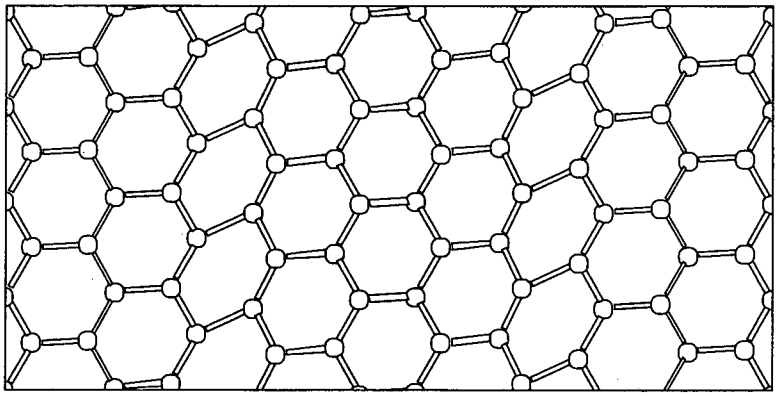

(a)

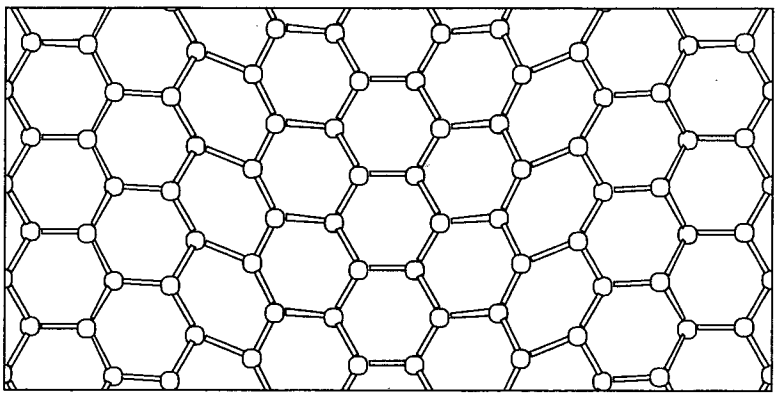

(b)

Figure 3.5: Two possible cells for a dipolar, SP-reconstructed unit cell, viewed from above the $(1\bar{1}1)$ plane: (a) same-sense reconstruction and (b) opposite-sense reconstruction. Shaded region indicates stacking fault.

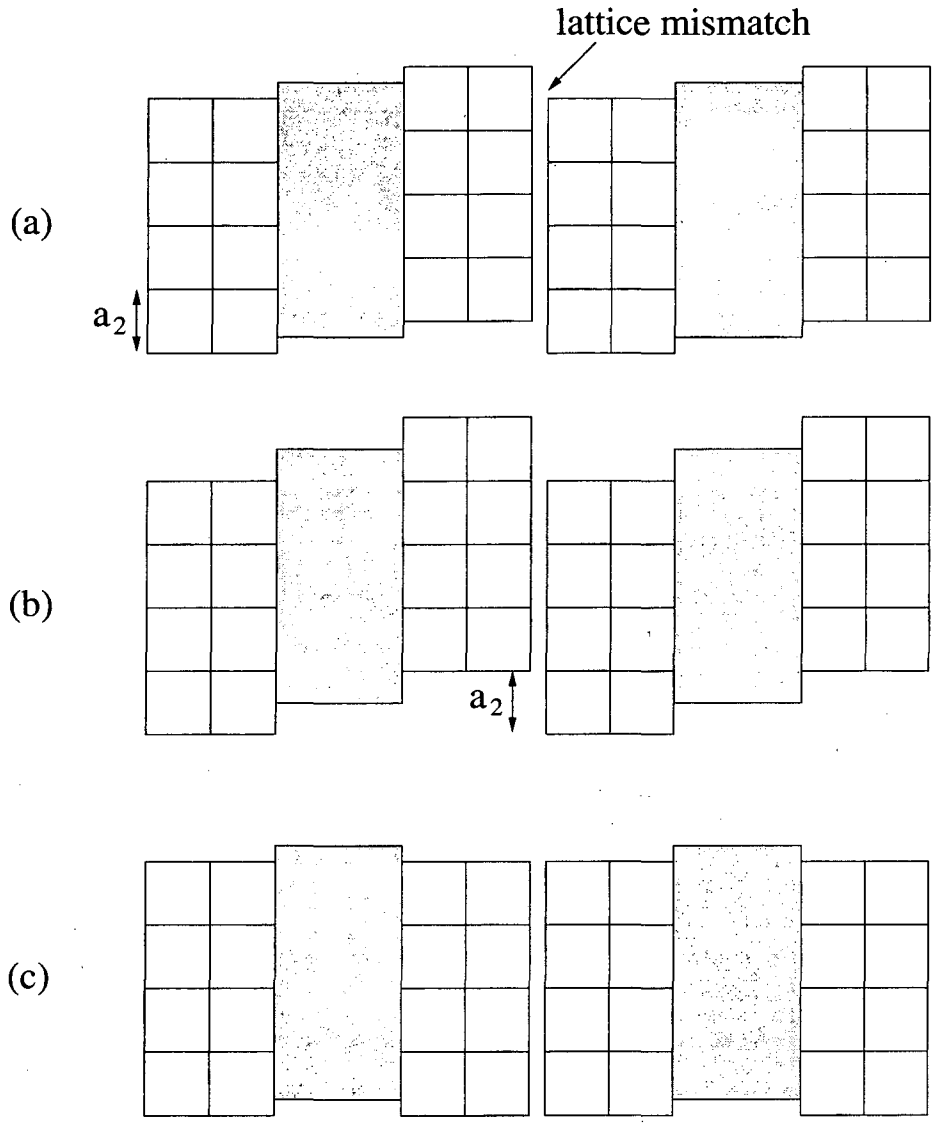

Figure 3.6: Schematic representation of same-sense and opposite-sense reconstructions of the dipolar unit cell, in the $(1\bar{1}1)$ plane. Shaded region indicates stacking fault. (a) For the same-sense reconstruction with arbitrary bond angles, lattice mismatch at the cell boundaries will occur. (b) This problem is avoided by constraining the bond angles in the dislocation core such that the regions on either side of the stacking fault are shifted by an integer multiple of $|\mathbf{a_3}|$. (c) The opposite-sense reconstruction requires no constraints on the bond angles.

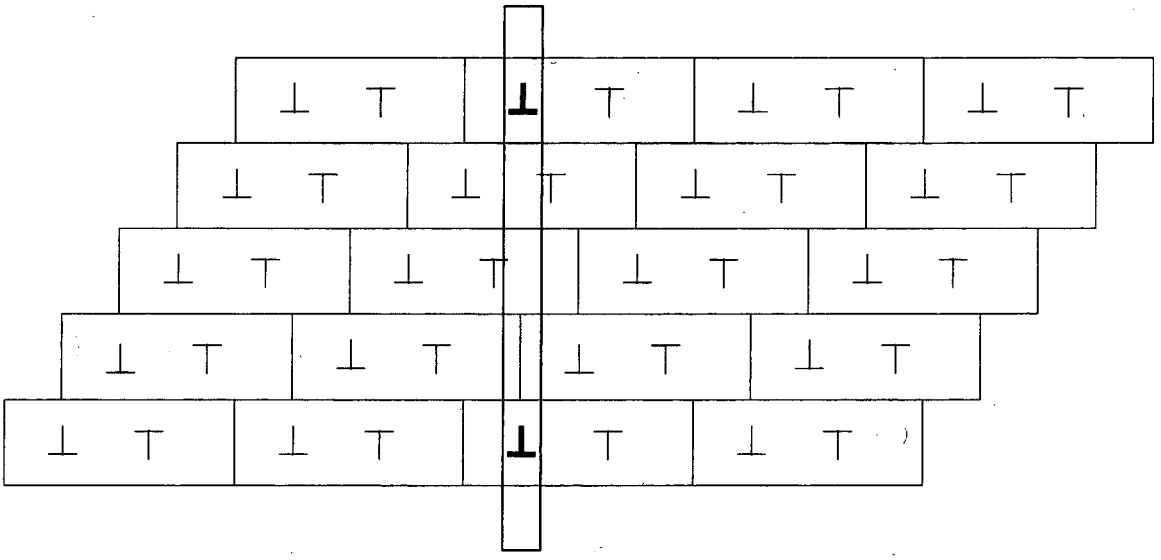

Figure 3.7: A periodic array of dislocations considered as a 1-D stack of tilt boundaries, viewed in the (110) plane.

where

$$\sigma_0 = \frac{\mu b}{2d(1-\nu)(\cosh 2\pi X - \cos 2\pi Y)^2} \tag{3.2}$$

and $X = x/d$, $Y = y/d$, where d is the distance between dislocations.

The self-energy of a tilt boundary is taken to be half the energy required to bring in the dislocation array from $x = \infty$ to $x = r_0$ against the stress field of a tilt boundary (of like sign) placed as in Figure 3.8. With $Y = 0$ (the tilt boundaries have no vertical offset), the shear stress σ_{xy} is

$$\begin{aligned} \sigma_{xy} &= \frac{\mu b}{2d(1-\nu)} \frac{2\pi X(\cosh 2\pi X - 1)}{(\cosh 2\pi X - 1)^2} \\ &= \frac{\mu b \pi}{2d^2(1-\nu)} \frac{x}{\sinh^2(\pi x/d)}. \end{aligned} \tag{3.3}$$

Since, in this coordinate system, $\mathbf{b} = (\mathrm{b}\ 0\ 0)$ and $\boldsymbol{\xi} = (0\ 0\ 1)$, the force in the x direction due to the presence of the first tilt boundary is found by the Peach-Koehler formula (Eq. 1.12) to be $F_x = b\sigma_{xy}$. The self-energy per dislocation per unit length is then related to the work required to overcome this force [6]

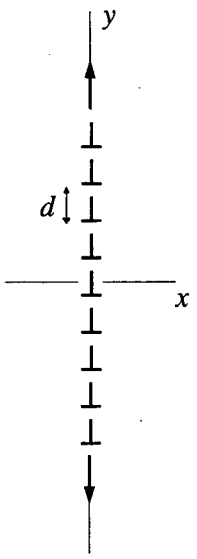

Figure 3.8: Coordinate system for Eqs. 3.1.

$$\begin{aligned} E_{self} &= -\frac{1}{2}\int_{\infty}^{r_0} b\sigma_{xy}\,dx \\ &= \frac{\mu b^2}{4\pi(1-\nu)}\left[\eta_0 \coth \eta_0 - \ln(2\sinh \eta_0)\right] \end{aligned} \tag{3.4}$$

where $\eta_0 = \pi r_0/d$.

The energy of a single dipolar unit cell is given by the self-energies of the two dislocations plus the interaction energy E_{int} between the two dislocations. However, since the dislocations are situated in an infinite array, E_{int} is actually the energy to assemble this array, per unit cell. The interaction energy (per dislocation per unit length) between two tilt boundaries separated by a distance x_0 and offset vertically by y_0 is, with $\zeta_0 = 2\pi x_0/d$, $Y_0 = y_0/d$, and $a = \cos 2\pi Y_0$,

$$\begin{aligned} \epsilon(x_0, y_0) &= -\frac{\mu b^2 \pi}{d^2(1-\nu)}\int_{\infty}^{x_0} \frac{x(a\cosh 2\pi x/d - 1)}{(\cosh 2\pi x/d - a)^2}\,dx \\ &= \frac{\mu b^2}{4\pi(1-\nu)}\left[\ln 2(\cosh \zeta_0 - a) - \frac{\zeta_0 \sinh \zeta_0}{\cosh \zeta_0 - a}\right] \end{aligned} \tag{3.5}$$

for same-signed boundaries, and $-\epsilon(x_0, y_0)$ for opposite-signed boundaries.

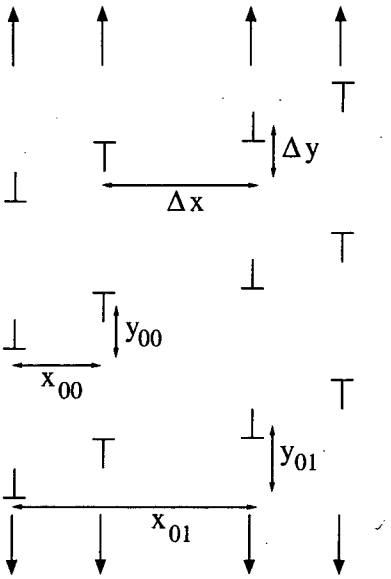

Figure 3.9: Definitions of the offsets x_{00}, y_{00}, x_{01}, and y_{01}, used in Eq. 3.7.

A formula for E_{int} can be now be determined. Let E^n_{tot} be the total elastic energy required to assemble n boundaries, given by

$$E^n_{tot} = \sum_i^n E_i \tag{3.6}$$

where E_i is the elastic energy required to add the *ith* boundary. Figure 3.9 shows the definitions for the tilt boundary offsets x_{00} and y_{00} for opposite-signed boundaries and x_{01} and y_{01} for same-signed boundaries, with $\Delta x = x_{01} - x_{00}$ and $\Delta y = y_{01} - y_{00}$. The offsets will depend on the cell parameters L, w, D, and T. (In practice, for the cells examined here, one will always find $x_{00} = 0$ and $y_{00} = d/2$.)

It is instructive to tabulate the first few E_i:

i	E_i
1	0
2	$-\epsilon(x_{00}, y_{00})$
3	$-\epsilon(\Delta x, \Delta y) + \epsilon(x_{01}, y_{01})$
4	$-\epsilon(x_{00}, y_{00}) + \epsilon(x_{01}, y_{01}) - \epsilon(x_{01} + x_{00}, y_{01} + y_{00})$
5	$-\epsilon(\Delta x, \Delta y) + \epsilon(x_{01}, y_{01}) - \epsilon(x_{01} + \Delta x, y_{01} + \Delta y) + \epsilon(2x_{01}, 2y_{01})$

The pattern can be easily discerned; it is

$$E_i = \begin{cases} E_{i-2} - \epsilon(\frac{i-3}{2}x_{01} + \Delta x, \frac{i-3}{2}y_{01} + \Delta y) + \epsilon(\frac{i-1}{2}x_{01}, \frac{i-1}{2}y_{01}) & i \text{ odd} \\ E_{i-2} + \epsilon(\frac{i-2}{2}x_{01}, \frac{i-2}{2}y_{01}) - \epsilon(\frac{i-2}{2}x_{01} + x_{00}, \frac{i-2}{2}y_{01} + y_{00}) & i \text{ even} \end{cases} . \quad (3.7)$$

The density of the dislocations in a tilt boundary will depend on the cell parameters L, D, w, and T. Since $\epsilon(x_0, y_0)$ is an energy *per dislocation* per unit length, the addition of two oppositely signed tilt boundaries corresponds to the addition of one unit cell only when the tilt boundary has maximum density, *i.e.* $d = D$. This is not the case in general, and it is never the case if the cell offset T is properly adjusted to relieve the elastic strain introduced by the dislocations as described above. To determine the elastic energy required to add a unit cell when $d = ND$, one must consider the energy required for the addition of $2N$ tilt boundaries, divided by N cells. Thus,

$$E_{int} = \lim_{m\to\infty} \frac{E_{tot}^{2mN} - E_{tot}^{2(m-1)N}}{N}. \quad (3.8)$$

The value for N is determined by the cell offset T, which can be written as a reduced fraction M/N of L. For example, for a quadrupolar array of cells with parameters $L = 6$, $D = 2$, and $w = 3$, the offset T is $L/2$ adjusted by $b(w/L)$. Since $b = |\mathbf{a_1}|/3$, $T = 6|\mathbf{a_1}|/2 + |\mathbf{a_1}|/6$, or $(\frac{1}{2} + \frac{1}{36})(6|\mathbf{a_1}|) = (19/36)L$. The density of dislocations in a tilt boundary will thus be $d = 36D$.

Once E_{int} has been determined, the energy to assemble the periodic array, per unit cell, is just

$$E_{cell} = 2E_{self} + E_{int}. \quad (3.9)$$

3.3 Analysis of *ab initio* calculations

3.3.1 Stress dependence of the stable core structure

The energy difference $\Delta E = E_{DP} - E_{SP}$ for various choices of cell parameters has been calculated by X. Blase [39] and is tabulated in Table 3.1, along with the stress components determined from isotropic elasticity theory using Eqs. 3.1. The

Table 3.1: Difference of energy $\Delta E = E_{DP} - E_{SP}$ (in meV/Å) between the double period (DP) and single period (SP) structures as a function of cell size and geometry, calculated by X. Blase [39]. The stresses σ_{xy}, σ_{xx}, and σ_{yy} on a dislocation, in units of $10^{-3}\mu$, are determined using isotropic elasticity theory.

L	D	w/L	σ_{xy}	σ_{xx}	σ_{yy}	ΔE
	$T/L = 0$					
4	2	1/2	0	0	0	-121
6	2	1/2	0	0	0	-128
6	2	1/3	6.69	-0.63	1.88	-120
6	2	1/4	16.2	-0.74	1.92	-69,-110†
4	3	1/2	0	0	0	-141
	$T/L = 1/2$					
4	2	1/2	0	0	0	-169
6	2	1/2	0	0	0	-198
6	2	1/3	27.7	0.63	-1.88	-161

†For this set of parameters, two different unit cells for the DP structure are possible, depending on whether the 5-membered ring faces a 7-membered ring or another 5-membered ring.)

energies were computed using density functional theory [48, 49] within the local density approximation [50, 51] and a non-local pseudopotential for carbon [52, 53]. The energy cutoff for the plane-wave expansion of the wavefunctions was 36 Ry, and the Brillouin zone was sampled by 4 **k**-points along the dislocation line for the SP cells and the equivalent 2 **k**-points for the DP cells.

Examination of Table 3.1 shows clearly that the observed energy difference ΔE depends on the choice of unit cell. The parameters $L = 4$, $D = 2$, $w/L = 1/2$, and $T/L = 1/2$ correspond to the cell used by Nunes *et al.* [43], and the result $\Delta E = -169$ meV/Å agrees with their LDA calculation that the DP cell is more stable than the SP cell (specifically, the more stable of the two possible SP cells, assumed to be the opposite-sense construction) by about 172 meV/Å. However, this number depends sensitively upon the choices of the cell parameters; for the same cell

in a dipolar configuration ($T/L = 0$), the energy difference decreases to 121 meV/Å.

Table 3.1 also demonstrates the sensitivity of the energy difference to the choice of w/L. For $L = 6$ and $D = 2$, the absolute value of ΔE decreases (*i.e.* the DP structure is stable by a smaller amount) as w is decreased. This trend is observed for both $T/L = 0$ and $T/L = 1/2$. The shear stresses on a dislocation in the periodic array, calculated within isotropic elasticity theory, are also observed to increase as w is decreased. These stresses can become quite large; for the case $T = L/2$, σ_{xy} is determined to be 0.028μ, or almost 15 GPa. The diagonal stresses, σ_{xx} and σ_{yy}, though smaller than the shear stress by about an order of magnitude, are nonetheless significant and may also affect the stable core structure. Finally, the variation of results for all the $w/L = 0$ cases, in which all the stress components are zero (due to the inversion symmetry of the array), suggests that ΔE depends not only on the stress, but also the stress gradients experienced by the dislocation.

3.3.2 Extraction of shear modulus and core radius

As shown in Section 3.2.3, the self-energy E_{self} depends on $\mu/(1-\nu)$ and the core radius r_0, and the interaction energy E_{int} depends on $\mu/(1-\nu)$. All other variables in the expression are determined by the cell parameters. Thus, it should be possible to use atomic scale energy calculations for various choices of unit cell to fit values for $\mu/(1-\nu)$ and r_0.

Table 3.2, in the column labeled E_{atom}, shows some *ab initio* energies for the SP reconstruction calculated by X. Blase [39]. Energies are per unit length of the dislocation, corrected for the stacking fault energy (calculated to be 17 meV/Å^2). The column labeled E_{fitted} lists the results of fitting to the isotropic elasticity theory energy expressions derived in Section 3.2.3, using μ and r_0 as fitting parameters. It is assumed that the core radius is independent of the stress experienced by the dislocation. For simplicity, the experimental value for ν for diamond cubic carbon 0.068 [6], is used; however, the results should be considered as fits to the prefactor $\mu/(1-\nu)$ and not μ alone. The shear modulus deduced from the fit is $\mu = 545 \pm 20$ GPa, in good agreement with the experimental value of 536 GPa quoted in Hirth and

Table 3.2: Comparison of atomic scale results (calculated by X. Blase [39]) and isotropic elasticity theory analysis. E_{atom} is the *ab initio* energy per unit length of the dislocation, corrected for the stacking fault energy. E_{fitted} is the same quantity calculated using elasticity theory and the fitted parameters. Energies are in eV/Å.

L	D	T/L	E_{atom}	E_{fitted}
	$w/L = 1/2$			
4	2	0	1.47	1.49
4	2	1/2	1.68	1.68
6	2	0	1.54	1.56
6	2	1/6	1.82	1.78
6	2	1/2	2.01	2.05
4	3	0	1.61	1.57
	$w/L = 1/3$			
6	2	0	1.54	1.52
6	2	1/2	1.92	1.90
	$w/L = 1/4$			
6	2	0	1.43	1.46
6	2	1/6	1.59	1.59
6	2	1/2	1.70	1.71

Lothe [6]. (Error bars are defined by the constant χ^2 boundary corresponding to a 90% confidence level.) The core radius deduced from the fit is $r_0 = 0.41 \pm 0.04$ Å, corresponding to $\alpha \approx 3.5$, which is also consistent with general expectations for the magnitudes of core radii [6].

Despite the assumptions that r_0 is independent of stress, and the inaccuracy of isotropic elasticity theory in certain applications, it is evident from the goodness of the fit that this simple combination of *ab initio* calculation and elasticity theory performs remarkably well in describing the energetics of dislocations in these infinite periodic arrangements. The largest discrepancy between the fitted values and the *ab initio* calculations is about 0.04 eV/Å, which translates into an uncertainty of only about 0.6 MPa in the stress required to bow a dislocation of length 1 μm to its critical configuration. Thus, the parameters μ and r_0 obtained are certainly adequate for inclusion into larger scale simulations.

3.4 Conclusions

The core structure and energy of the 90° partial dislocation in diamond has been studied using a combination of *ab initio* calculations and elasticity theory analysis. The relative energies of two possible reconstructions of the dislocation core are examined within a periodic supercell framework, and it is found that the double period reconstruction is more stable for a wide range of stress states. A method for calculating the energy per unit length of a dislocation in the periodic array is introduced and used to fit values for the shear modulus μ of diamond and the core radius r_0 of the 90° partial. The results are found to agree well with experimental observations and theoretical estimates, thus suggesting that *ab initio* techniques may be used to provide accurate parameters for larger continuum theory simulations.

The notion that the stable core structure of a dislocation depends on the environment in which it is located has already been introduced by Lehto and Öberg [45], but this combination of total energy calculation and elasticity theory analysis now provides a way of studying this dependence systematically. The trends observed in Table 3.1 suggest a detailed examination of the relative stability of the two possible

reconstructions, in which many different unit cells are used to place the dislocation under a wide range of stress states. This analysis, as well as a comparison with the method of cylindrical cluster boundary conditions, is presented for the 90° partial dislocation in silicon in the next chapter.

Chapter 4

The 90° partial dislocation core in silicon†

The analysis of the 90° partial dislocation in diamond presented in the last chapter revealed that the double-period reconstruction of the dislocation core is more stable than the previously assumed single-period reconstruction, but by an amount that depends on the stress state of the dislocation. Since silicon has a crystal structure identical to that of diamond, it is expected that similar trends will be observed. In fact, the 90° partial dislocation in silicon has received comparatively more attention than that in diamond, perhaps due to the technological importance of silicon and the impact of defects on the electronic properties of silicon-based devices.

As previously mentioned, the DP structure was originally proposed and found to be lower in energy than the SP structure in silicon by Bennetto *et al.* [42] in 1997, using the method of periodic supercells with $L = 4$, $D = 3$, $w/L = 1/2$, and $T/L = 1/2$ (see Section 3.2.2 for parameter definitions). However, it was pointed out by Lehto and Öberg [45] in 1998 that the two structures are very close in energy, and the results depend sensitively on the environment in which the dislocation is located. Valladares *et al.* [46] also noted that at temperatures where dislocations are mobile, the difference between free energies of the SP and DP cores is insignificant and both structures should be present.

†Most of the research presented in this chapter has been submitted for publication (Ref. [54]).

The observations of these authors, as well as the work on diamond reported in the previous chapter, suggest that theoretical calculations of dislocation core energies must carefully take into account the effects of the chosen boundary conditions. The work presented in this chapter aims to perform such a study. Using a combination of total energy calculations and elasticity theory analysis similar to that described in the last chapter, the relative stability of the SP and DP core structures of the 90° partial dislocation in silicon is examined. Both cylindrical cluster and periodic boundary conditions are employed and the results compared. It is argued that the relative stability of the two reconstructions depends on the stress state of the dislocation, and this dependence is studied systematically using periodic supercells.

4.1 The Tersoff potential

While *ab initio* calculations such as those employed in the previous chapter provide the most accurate energies of atomic systems, the computational power and time required to perform such calculations make them unfeasible for studies of more than several hundred atoms at a time. Since the goal of the current work is to examine a large variety of boundary conditions in order to place the dislocation under a wide range of stress states, the accuracy of *ab initio* methods is traded for the simplicity and speed of empirical interatomic potentials, in which the energy is modeled as a sum of few-body interactions with parameters determined by best fit to experiment; perhaps the best known of these is the Lennard-Jones "6-12" potential. While one will ultimately desire to use the most accurate total energy techniques available, the use of empirical potentials provides a good compromise for a first look at the quantities of interest.

The empirical potential chosen in this work is the Tersoff potential for covalent systems [55], which has been optimized for silicon and gives a good description of its elastic properties [56, 57]. The Tersoff potential models the energy as a sum of pairlike interactions, but with a term that depends on bond angle, thus incorporating the effect of the local environment on the strength of a given bond. The form of the energy is

$$\begin{aligned} E &= \frac{1}{2}\sum_{i\neq j} V_{ij} \\ V_{ij} &= f_c(r_{ij})[a_{ij} f_R(r_{ij}) + b_{ij} f_A(r_{ij})] \end{aligned} \tag{4.1}$$

where i and j label atoms of the system and r_{ij} is the distance between atoms i and j, *i.e.* the length of the bond ij. The functions $f_R(r)$ and $f_A(r)$ are repulsive and attractive terms, respectively, and decrease exponentially with r. The coefficient of the attractive term, b_{ij}, depends on the angles between the bond ij and the other bonds ik, where $k \neq j$ labels the other neighbors of atom i. Finally, $f_c(r)$ is a cutoff function defined by

$$f_c(r) = \begin{cases} 1 & r < R - D \\ \frac{1}{2} - \frac{1}{2}\sin\left[\frac{\pi}{2}(r-R)/D\right] & R - D < r < R + D \\ 0 & r > R + D \end{cases} \tag{4.2}$$

where R and D are empirical parameters, optimized for silicon to be $R = 2.85$ Å and $D = 0.15$ Å [56, 57]. The Tersoff potentials are implemented using a modified version of the Ames Lab Classical Molecular Dynamics (AL_CMD) code.

4.2 Periodic boundary conditions

4.2.1 Extraction of shear modulus and core radius

The same combination of total energy calculations and isotropic elasticity theory performed for diamond in the last chapter (Section 3.3.2) is repeated here for silicon, but with the *ab initio* calculations replaced by Tersoff potential calculations. Three choices of unit cell in the SP reconstruction are employed: $L = 12$, $D = 3$; $L = 6$, $D = 2$; and $L = 6$, $D = 8$, in both the dipolar ($T/L = 0$) and quadrupolar ($T/L = 1/2$) arrangements, with w varied from 1 to $L - 1$. It is assumed again that the core radius r_0 is independent of stress, and the experimental value for ν for silicon is used, 0.218 [6]. The results of the fit are shown in Figure 4.1, with $\mu = 55 \pm 13$ GPa

and $r_0 = 0.67 \pm 0.05$ Å. The value for μ is in agreement with both the experimental value of 68.1 GPa [6] and the value predicted by the Tersoff potentials, 54.8 GPa [56]. The core radius r_0 corresponds to $\alpha \approx 3.3$. This is not too far from the result $\alpha = 4.08$ found by Trinczek and Teichler [58]; the discrepancy is likely due to their use of a different potential, an older bond charge model introduced by Weber [59].

4.2.2 Stress dependence of the stable core structure

By employing Eqs. 3.1 along with Tersoff potential calculations of $\Delta E = E(DP) - E(SP)$, the difference in core energies for the SP and DP reconstructions as a function of stress can now be studied systematically. Most previous attempts at identifying the stable core structure [42, 43, 46] were restricted to a quadrupolar cell. While the stress field on a dislocation in this arrangement is indeed zero, it will be shown that the relative stability of the two core structures depends not only on the stress but also the stress gradients. The present work uses several unit cells to place the dislocation under a variety of stress states which can be determined with isotropic elasticity theory analysis. In this manner, the dependence of the energy difference on the dislocation environment can be quantified.

Figure 4.2 shows the predicted difference in core energies, E(DP)-E(SP), as a function of the shear stress σ_{xy}. The shear stress is varied for a given cell by changing w, which can range from 1 to $L-1$. The stresses thus obtained, for the cells under consideration, can be as large as 0.07μ, or almost 4 GPa. It is clear from the plot that the energy difference depends sensitively and systematically on the stress field experienced by the dislocation. Although the DP core is more stable than the SP core for most stresses, in general the energy difference decreases with increasing σ_{xy}.

The lack of coincidence of the curves suggests that the relative stability of the two reconstructions depends on more than the shear stress. For the cell $L = 6, D = 2$, the points corresponding to $w/L = 1/2$ are those for which $\sigma_{xy} = 0$ (as is the case for all the cells), but as seen from Figure 4.2, ΔE is nearly zero (suggesting that the DP and SP cores are equally stable) for $T = 0$ but is ≈ -15 meV/Å for $T = L/2$. The

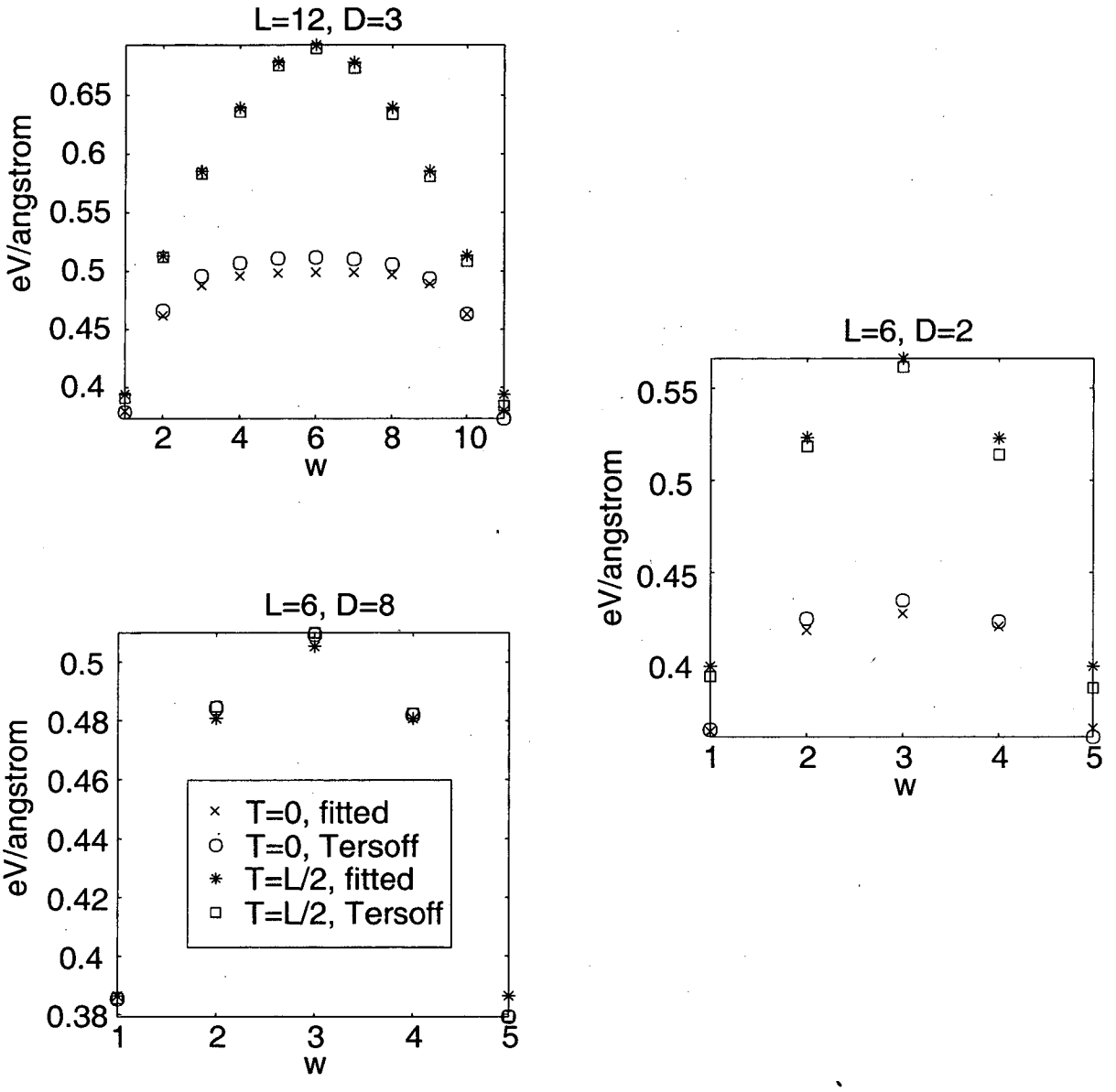

Figure 4.1: Fits to isotropic elasticity theory of total energy calculations for the SP core from Tersoff potentials, using periodic boundary conditions for three different unit cells. Data are fit simultaneously, assuming μ and r_0 do not change with unit cell.

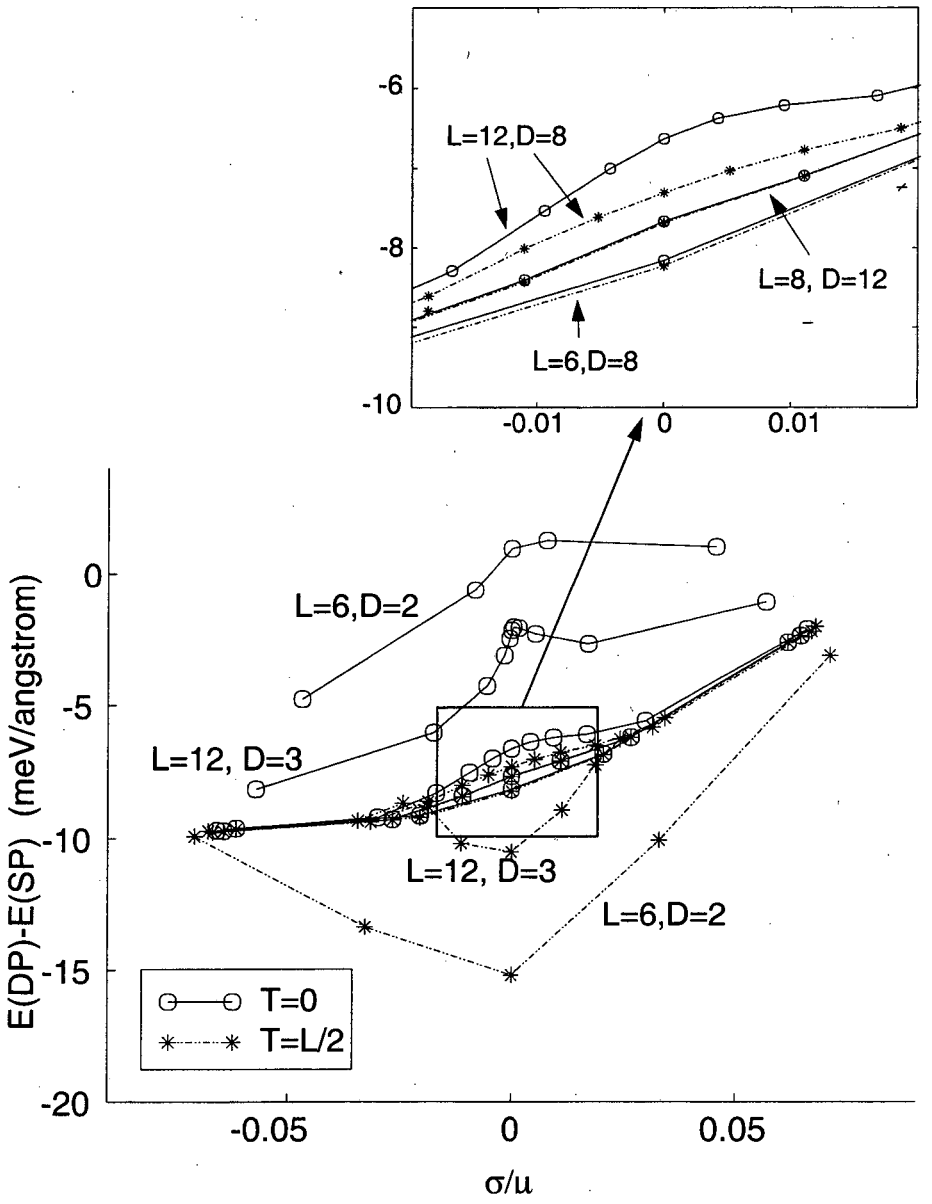

Figure 4.2: Energy difference E(DP)-E(SP) for silicon as a function of shear stress for various choices of unit cell. A negative number indicates that the DP structure is more stable.

difference is due to the stress *gradients*, which are different for the two cases.

The diagonal stress components σ_{xx} and σ_{yy} and their gradients are also affected by the periodic arrangement of the dislocations. The two most outlying curves, corresponding to the cell with dimensions $L = 6, D = 2$, have the largest diagonal stress components for $w/L \neq 1/2$ (up to half the magnitude of the shear stress), whereas the curves $L = 6, D = 8$ and $L = 8, D = 12$ place the dislocation under a stress state much closer to pure shear (σ_{xx} and σ_{yy} are $\approx 10^{-5}\sigma_{xy}$). This suggests that the small cells used by previous workers [42, 46] to determine the relative stability of the SP and DP cores may subject the dislocations to stress field conditions that drastically affect the observed value of the energy difference E(DP)-E(SP). This dependence of ΔE on the stresses and stress gradients experienced by the dislocation confirm and quantify the observation of Lehto and Öberg [45] that the relative stability of the two cores is highly dependent on the environment in which the dislocation is located.

4.3 Cylindrical boundary conditions

Up to now, the stable core structure of the 90° partial dislocation has been examined in this work using only periodic boundary conditions. Another possibility found in the literature [45, 60] is to use cylindrical boundary conditions, which treat a single dislocation in the following manner. A cylindrical cluster of atoms around the dislocation line is generated, with initial positions determined by anisotropic elasticity theory. The atoms on the surface of the cylinder are fixed, and the remaining atoms around the dislocation line are allowed to relax. Figure 4.3 illustrates a typical atomic configuration, viewed along the dislocation line.

Unlike the case of periodic supercells, the initial placement of the dislocation is important because it determines for all time the positions of the outer atoms. However, the attempt to treat a discrete atomic lattice with continuum elasticity theory introduces an ambiguity; a dislocation's position can only be defined down to the interatomic spacing. While one approach is simply to place the dislocation on the center axis of the cylinder, the lack of perfect radial symmetry about this axis at the

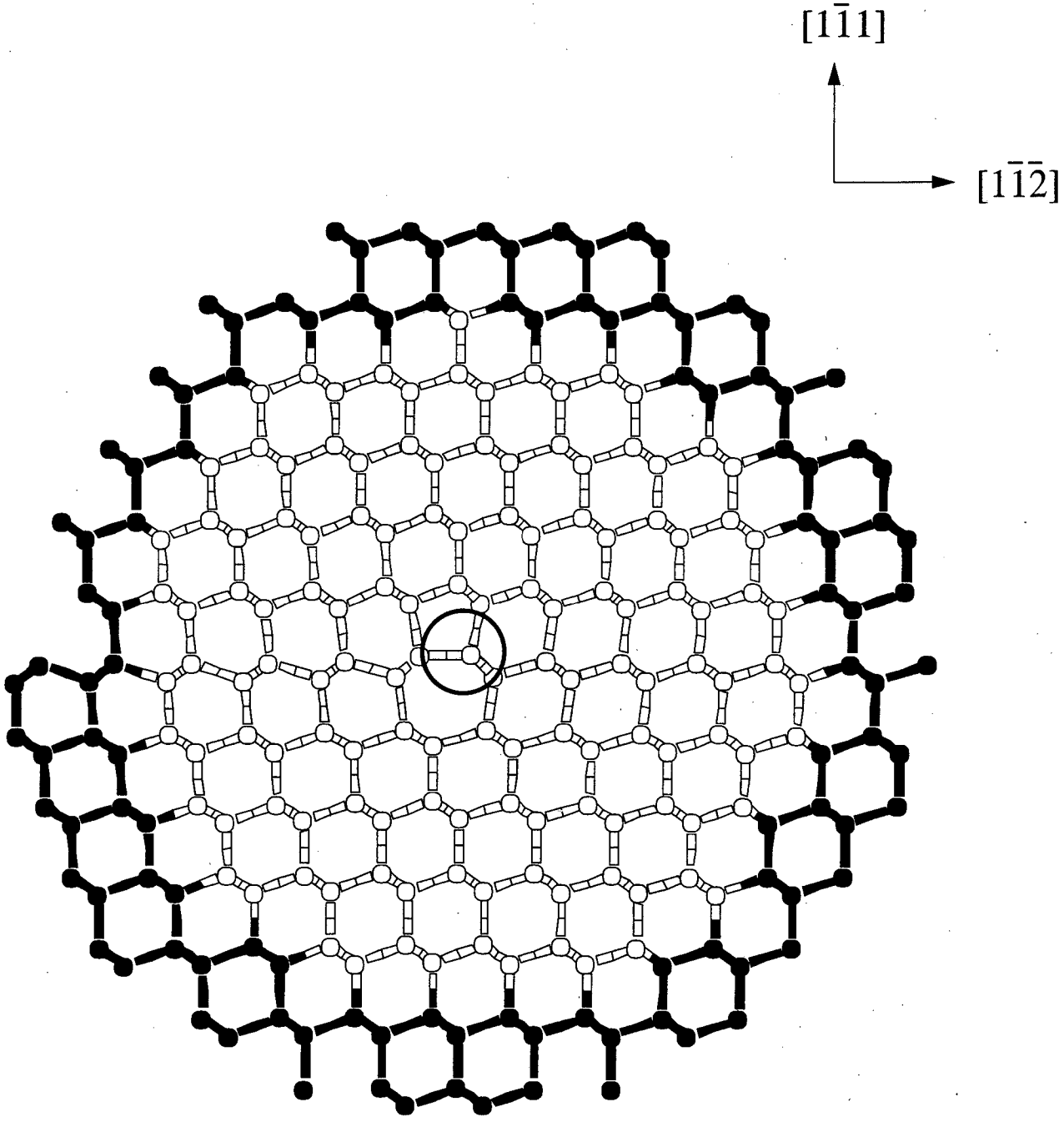

Figure 4.3: Illustration of a cylindrical cell, viewed from above the (110) plane. Surface atoms, held fixed during relaxation, are shown darker. The dislocation position is optimized within a circle of radius b (shown) about the center of the cylinder.

atomic level suggests that the core energy of the relaxed configuration may be lower if the dislocation is displaced slightly from this axis. Further, there is no reason to assume that the optimal position for the dislocation is the same for the SP and DP structures.

In order to explore these issues more carefully, the following procedure is performed. The trial cylinder is taken to have a radius of 20 Å and is periodic along the dislocation line direction. Atoms within 5 Å of the surface are held fixed. For each core reconstruction, the dislocation position is varied in increments of 0.1 Å along each direction within a circle of radius b, where b is the magnitude of the Burgers vector (about 2.2 Å). The resulting configurations are relaxed using Tersoff potentials and the energies recorded. For the SP core, the optimal placement of the dislocation is found to be $x = -1.4$, $y = -0.5$, where the x-axis is in the $[1\bar{1}\bar{2}]$ direction and the y-axis is in the $[1\bar{1}1]$ direction. For the DP core, the optimal position is $x = 0.3$, $y = -0.7$. The energy differences associated with the placement of the core can be significant, resulting in variations of $\Delta E = E(DP) - E(SP)$ of up to 5 meV/Å. These variations are on the order of ΔE itself, calculated using the same Tersoff potential.

As the radius of the cylinder is increased and surface effects become less significant, ΔE is expected to approach a value close to what is expected for an isolated dislocation in a bulk material. Figure 4.4 plots ΔE as a function of cylinder radius, using the optimal positions for the SP and DP cores as determined above. The thickness of the outer cylinder of fixed atoms is kept constant at 5 Å; supplemental trials suggest that variations in this thickness are insignificant, especially as the cylinder radius is increased.

As the radius of the cylinder increases, $E(DP) - E(SP)$ approaches a value of approximately -6.8 meV/Å. This result is to be compared to the zero shear stress, or $w = L/2$, case in the periodic calculations shown in Figure 4.2. Although this number varies among the choices of unit cell, it is reasonable to choose the points corresponding to the largest cells, in which the dislocations are the most isolated (albeit with separations on the order of tens of angstroms). The cells $L = 12$, $D = 8$ and $L = 8$, $L = 12$ show $E(DP) - E(SP)$ from -6.5 to -8 meV/Å. Thus, it can be concluded that the periodic supercell method gives results comparable to those from

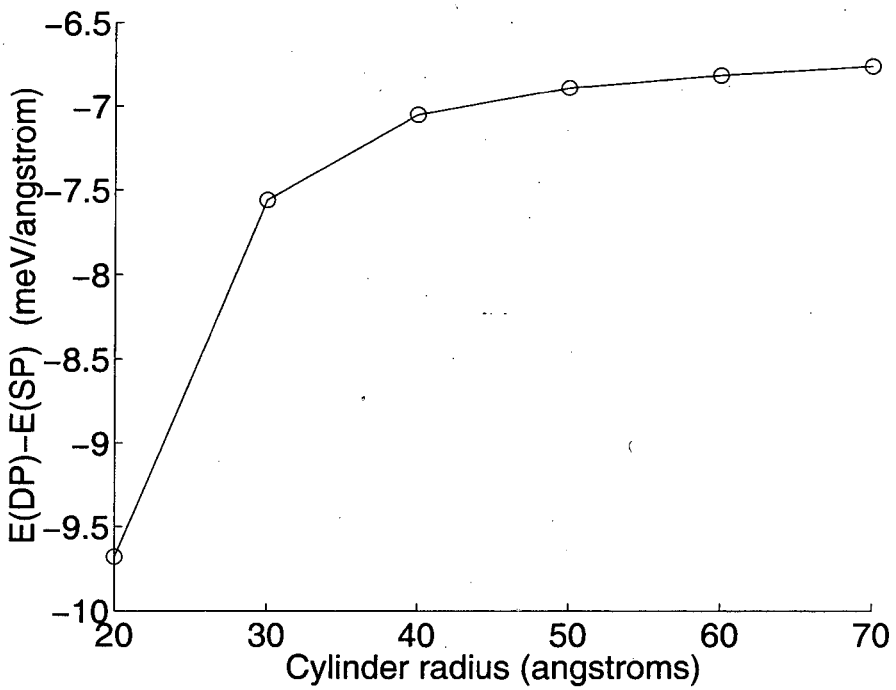

Figure 4.4: Energy difference E(DP)-E(SP) for silicon, calculated using Tersoff potentials and cylindrical boundary conditions, as a function of the cylinder radius.

cylindrical cluster calculations in the case of an isolated dislocation, provided that the periodic cell is chosen judiciously.

4.4 Pressure calculations

The effects of the diagonal stress components σ_{xx} and σ_{yy} on the relative stability of the SP and DP cores, as shown in Figure 4.2 and discussed in Section 4.2.2, suggest that one may be able to induce a transition where the SP core is more stable by applying a hydrostatic pressure to the periodic unit cells. This is accomplished in the following manner. A number of perfect diamond cubic cells are generated with lattice constants varying near the lattice constant $a = 5.43$ for Si. The energy of these unit cells, calculated using Tersoff potentials, is then tabulated and a cubic spline is fit to the E vs. V curve. Since $P = -\partial E/\partial V$, it is then possible to extract the lattice constant corresponding to a particular pressure. This lattice constant is then used to generate the dipolar, two-dislocation unit cells. As a check on how well the Tersoff potentials perform in this context, the bulk modulus $B = V(\partial^2 E/\partial V^2)$ for silicon is calculated and found to be 107.2 GPa, in reasonable agreement with the experimental value of 98.8 GPa [26].

Since

$$P = -\frac{1}{3}(\sigma_{xx} + \sigma_{yy} + \sigma_{zz}), \tag{4.3}$$

the diagonal stress components are simply

$$\sigma_{xx} = \sigma_{yy} = \sigma_{zz} = -P \tag{4.4}$$

for hydrostatic pressure. Figure 4.5 shows the results of applying pressure to the $L = 6$, $D = 8$ cell, for which the diagonal stress components are normally very small. (The difference between the $T/L = 0$ and $T/L = 1/2$ curves is negligible on the scale of the plot.) As the diagonal stress components are increased, the curve moves up on the plot, indicating that the DP core is becoming less stable with respect to the SP core. For $P = 3$ GPa, the SP core appears to be more stable for all but the most extreme shear stresses.

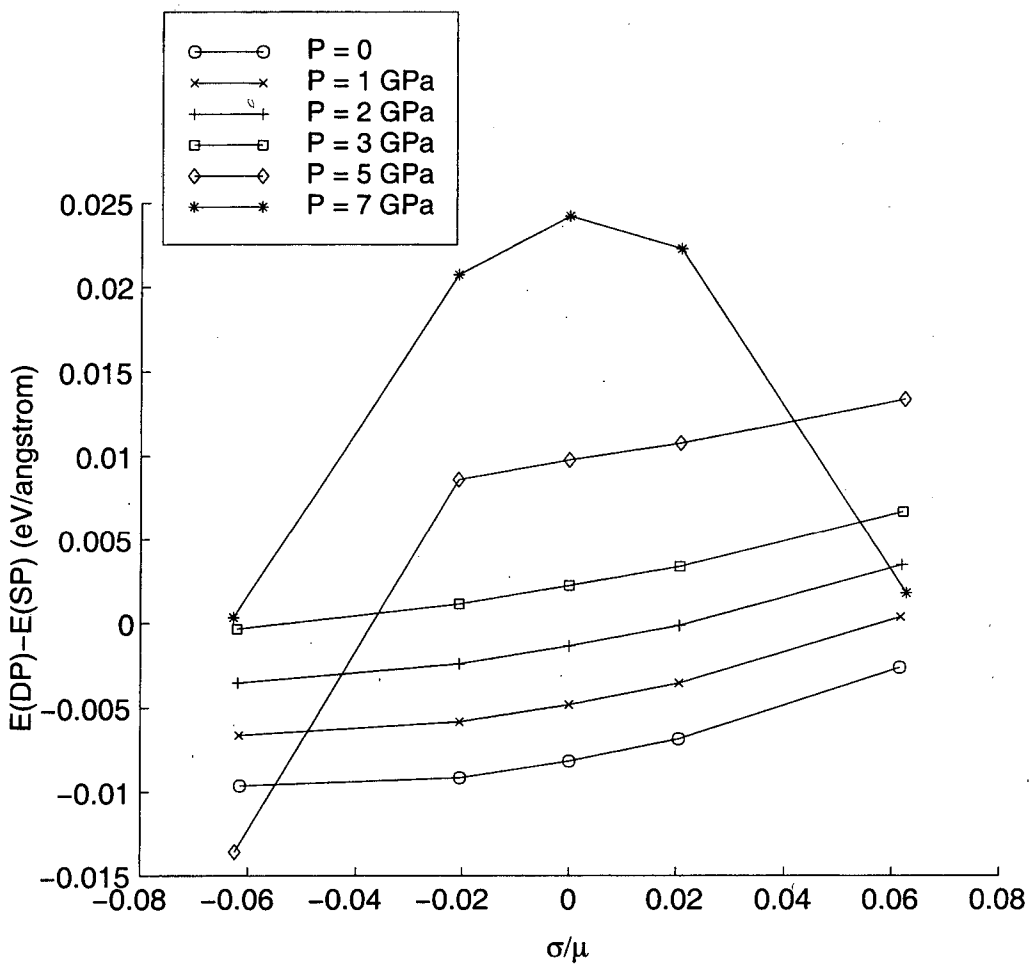

Figure 4.5: Plots of $\Delta E = E(DP) - E(SP)$ for the $L = 6$, $D = 8$ cell, with a hydrostatic pressure imposed. As the pressure is increased, the DP core becomes less stable with respect to the SP core.

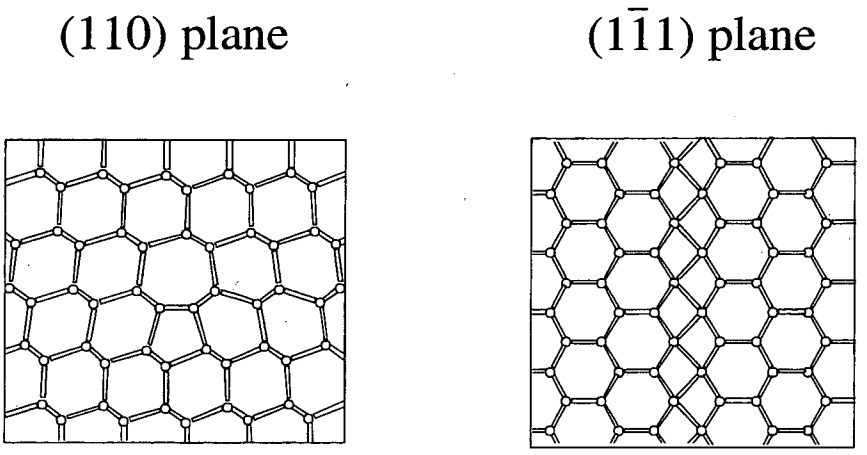

Figure 4.6: Symmetric, quasi-fivefold coordinated reconstruction of the 90° partial dislocation viewed from above the (110) and (1$\bar{1}$1) planes. Shaded area indicates stacking fault.

For values of P of 5 GPa and above, the curves begin to take on a different shape. Examination of the relaxed core structures reveals that this is due to yet another transition; the SP core has transformed into a *symmetric* reconstruction, in which each atom along the core has three first neighbors and two further neighbors at a distance 17% greater than the equilibrium bond length (See Figure 4.6). In this structure, found by Duesbery *et al.* [61], the atoms are said to have "quasi-fivefold" coordination. The bonds across the dislocation core are longer in the quasi-fivefold coordinated symmetric core than in the four-fold coordinated asymmetric core. For the cells under zero or low pressure, the symmetric reconstruction is metastable and transforms spontaneously to the unreconstructed core (Figure 3.2(a)) which is significantly higher in energy than both the DP core and the asymmetric SP core.

Although Duesbery *et al.* found the symmetric reconstruction to be more stable using certain empirical potentials [62, 63], it was later determined by Bigger *et al.* [47] using more accurate *ab initio* techniques that the asymmetric reconstruction (Figure 3.2(b)) is in fact more stable, and it is thus this reconstruction for the SP

core that has been considered in the most recent literature. However, the inability of other empirical potentials to predict the correct SP reconstruction suggests that the transition seen here is similarly an artifact of the Tersoff potential and its limited range. As the pressure is increased, the lattice constant and hence the average bond length decreases. When the lattice constant becomes small enough, more atoms may fall within the $R+D = 3$ Å cutoff defined by the Tersoff parameters for silicon for the function $f_c(r)$ in the pair interaction of Eq. 4.1, making the symmetric reconstruction (with five neighbors rather than four) more energetically favorable.

Since the Tersoff potentials are likely to be inadequate for resolving energy differences at this small of a scale anyway, the calculations should be repeated using more accurate methods. Nonetheless, if the trend observed in Figure 4.5 is correct, this suggests that the stable core structure may change from DP to SP upon application of an external pressure. If electronic states of the two cores can be identified so as to allow one to distinguish them experimentally, it may be possible to observe this transition directly.

4.5 Conclusions and future work

A study of the core structure of the 90° partial dislocation in silicon has been performed using periodic supercells and cylindrical cluster boundary conditions. The two types of boundary conditions are compared and found to agree well in the case of an isolated dislocation. The relative stability of the single-period and double-period constructions of the core is found to depend systematically on the stress state experienced by the dislocation, and this dependence is quantified using a combination of empirical total energy calculations and isotropic elasticity theory. The DP core reconstruction is found to be more stable for most choices of unit cell, but a transition to the SP core may be observed under the application of a hydrostatic pressure.

Several obvious directions exist for expansion on the work presented in this and the previous chapter. First, the calculations performed on silicon should be repeated with better techniques, since empirical potentials are unlikely to be accurate enough to resolve differences on the scale required for this type of analysis. Second,

while isotropic elasticity theory has performed admirably in extracting values for the shear modulus and core radius, the data fits as well as the stress calculations could be improved by using anisotropic elasticity theory. Finally, it is expected that the techniques developed here can be applied equally well to other types of dislocations, such as the 30° partial and the undissociated screw dislocation.

Appendix A

Solution of the free surface equation

This appendix gives the detailed solution of Eq. 2.16:

$$\frac{\partial y}{\partial t} = D\frac{\partial^2 y}{\partial x^2} + \alpha \sum_{n=-\infty}^{\infty} \delta(x - nL) + \beta. \tag{A.1}$$

Begin by switching to dimensionless units:

$$Y = y/L \tag{A.2}$$

$$X = x/L \tag{A.3}$$

$$D' = D/\alpha \tag{A.4}$$

$$\tau = \alpha t/L^2 \tag{A.5}$$

Substituting into Eq. A.1 yields

$$\frac{\partial Y}{\partial \tau} = D'\frac{\partial^2 Y}{\partial X^2} + \sum_{n=-\infty}^{\infty} \delta(X - n) + \frac{\beta L}{\alpha}. \tag{A.6}$$

The last term can be ignored for now, since it will just provide a contribution linear in τ. The periodicity imposed by the delta function summation suggests a solution of the form

$$Y(X,\tau) = \sum_{m=-\infty}^{\infty} a_m e^{i(2\pi m X)} f_m(\tau) \tag{A.7}$$

which upon substitution into Eq. A.6 becomes

$$\sum_{m=-\infty}^{\infty} a_m e^{i(2\pi m X)} \left\{ \frac{df_m(\tau)}{d\tau} + D'(2\pi m)^2 f_m(\tau) - \frac{1}{a_m} \right\} = 0. \tag{A.8}$$

The expression in brackets must be identically zero, leading to a solution of $f_m(\tau)$ of the form

$$f_m(\tau) = A_m e^{-4\pi^2 m^2 D'\tau} + B_m. \tag{A.9}$$

Using Eq. A.8 and the initial condition $y(x,0) = 0 \Rightarrow f_m(0) = 0$, the constants A_m and B_m are found to be

$$B_m = \frac{1}{4\pi^2 m^2 D' a_m} \tag{A.10}$$

$$A_m = -B_m \tag{A.11}$$

Finally, substitution of Eq. A.9 back into Eq. A.7 yields

$$\begin{aligned} Y(X,\tau) &= \sum_{m=-\infty}^{\infty} \frac{e^{i(2\pi m X)}}{4\pi^2 m^2 D'} (1 - e^{-4\pi^2 m^2 D'\tau}) + \frac{\beta L}{\alpha}\tau \\ &= \tau + \sum_{m=1}^{\infty} \frac{\cos 2\pi m X}{2\pi^2 m^2 D'} (1 - e^{-4\pi^2 m^2 D'\tau}) + \frac{\beta L}{\alpha}\tau \end{aligned} \tag{A.12}$$

where the contribution from the last term in Eq. A.6 is now included. Upon transforming back into the original units,

$$y(x,t) = \left(\frac{\alpha}{L} + \beta\right) t + \frac{\alpha L}{2\pi^2 D} \sum_{m=1}^{\infty} \frac{cos(2\pi m x/L)(1 - e^{-4D\pi^2 m^2 t/L^2})}{m^2}. \tag{A.13}$$

Bibliography

[1] J. Frenkel, Zeitschrift für Physik **37**, 572 (1926).

[2] E. Orowan, Zeitschrift für Physik **89**, 605, 634 (1934).

[3] M. Polanyi, Zeitschrift für Physik **89**, 660 (1934).

[4] G. I. Taylor, Proceedings of the Royal Society **A145**, 362 (1934).

[5] J. M. Burgers, Proceedings of the Koninklijke Nederlandse van Wetenschappen **42**, 293, 378 (1939).

[6] J. P. Hirth and J. Lothe, *Theory of Dislocations*, 2nd ed. (John Wiley & Sons, New York, 1982).

[7] F. C. Frank and A. J. Forty, Proceedings of the Royal Society **A217**, 262 (1953).

[8] W. C. Dash, in *Dislocations and Mechanical Properties of Crystals* (Wiley, New York, 1957), p. 57.

[9] D. Hull and D. J. Bacon, *Introduction to Dislocations*, 3rd ed. (Pergamon Press, Oxford, 1984).

[10] R. E. Peierls, Proceedings of the Physical Society **52**, 23 (1940).

[11] F. R. N. Nabarro, Proceedings of the Physical Society **59**, 256 (1947).

[12] F. R. N. Nabarro, Philosophical Magazine A **75**, 703 (1997).

[13] A. Seeger and P. Schiller, in *Physical Acoustics*, edited by W. P. Mason (Academic, New York, 1966), Vol. 3A, p. 361.

[14] M. O. Peach and J. S. Koehler, Physical Review **80**, 436 (1950).

[15] C. B. Carter and S. M. Holmes, Philosophical Magazine **35**, 1161 (1977).

[16] A. Gomez, D. J. H. Cockayne, P. B. Hirsch, and V. Vitek, Philosophical Magazine **31**, 105 (1975).

[17] H. R. Kolar, J. C. H. Spence, and H. Alexander, Physical Review Letters **77**, 4031 (1996).

[18] L. P. Kubin *et al.*, Solid State Phenomena **23/24**, 455 (1992).

[19] M. Tang, L. P. Kubin, and G. R. Canova, Acta Materialia **46**, 3221 (1998).

[20] L. P. Kubin, A. Moulin, and P. Pirouz, in *Multiscale Modelling of Materials* (Materials Research Society, Boston, MA, 1999), Vol. 538, p. 3.

[21] K. W. Schwarz, Journal of Applied Physics **85**, 108 (1999).

[22] M. Rhee, Modelling and Simulation in Materials Science and Engineering **6**, 467 (1998).

[23] N. M. Ghoniem, Physical Review B **61**, 913 (2000).

[24] A. K. Faradjian, L. H. Friedman, and D. C. Chrzan, Modelling and Simulation in Materials Science and Engineering **7**, 479 (1999).

[25] K. Lin and D. C. Chrzan, Physical Review B **60**, 3799 (1999).

[26] C. Kittel, *Introduction to Solid State Physics*, 6th ed. (John Wiley & Sons, New York, 1986).

[27] P. A. Maksym, Semiconductor Science and Technology **3**, 594 (1988).

[28] A. Granato and K. Lücke, Journal of Applied Physics **27**, 583 (1956).

[29] T. Suzuki, H. Koizumi, and H. O. K. Kirchner, Acta Metallurgica et Materialia **43**, 2177 (1995).

[30] S. Nemat-Nasser and J. B. Isaacs, Acta Materialia **45**, 907 (1997).

[31] J. W. Christian, Metallurgical Transactions A **14A**, 1237 (1983).

[32] J. C. M. Li, Philosophical Magazine **10**, 1097 (1964).

[33] Y. Maurissen and L. Capella, Philosophical Magazine **29**, 1227 (1974).

[34] Y. Maurissen and L. Capella, Philosophical Magazine **30**, 679 (1974).

[35] M. Kardar, G. Parisi, and Y. C. Zhang, Physical Review Letters **56**, 889 (1986).

[36] F. Family and T. Vicsek, Journal of Physics A **18**, 75 (1985).

[37] J. Krug and H. Spohn, in *Solids Far From Equilibrium*, edited by C. Godrèche (Cambridge University Press, Cambridge, 1992).

[38] S. F. Edwards and D. R. Wilkinson, Proceedings of the Royal Society of London **1**, 1 (2000).

[39] X. Blase *et al.* (submitted for publication).

[40] P. B. Hirsch, Journal de Physique (Paris) Colloque **40**, C6 (1979).

[41] P. B. Hirsch, Journal de Physique (Paris) Colloque **40**, C6 (1979).

[42] J. Bennetto, R. W. Nunes, and D. Vanderbilt, Physical Review Letters **79**, 245 (1997).

[43] R. W. Nunes, J. Bennetto, and D. Vanderbilt, Physical Review B **58**, 12563 (1998).

[44] T. A. Arias and J. D. Joannopoulos, Physical Review Letters **73**, 680 (1994).

[45] N. Lehto and S. Öberg, Physical Review Letters **80**, 5568 (1998).

[46] A. Valladares, A. K. Petford-Long, and A. P. Sutton, Philosophical Magazine Letters **79**, 9 (1999).

[47] J. R. K. Bigger *et al.*, Physical Review Letters **69**, 2224 (1992).

[48] P. Hohenberg and W. Kohn, Physical Review **136**, B864 (1964).

[49] W. Kohn and L. J. Sham, Physical Review **140**, A1133 (1965).

[50] D. M. Ceperley and B. J. Alder, Physical Review Letters **45**, 566 (1980).

[51] J. P. Perdew and A. Zunger, Physical Review B **23**, 5048 (1981).

[52] K. Kleinman and D. M. Bylander, Physical Review Letters **48**, 1425 (1982).

[53] N. Troullier and J. L. Martins, Solid State Communications **74**, 613 (1990).

[54] K. Lin and D. C. Chrzan (submitted for publication).

[55] J. Tersoff, Physical Review B **37**, 6991 (1988).

[56] J. Tersoff, Physical Review B **38**, 9902 (1988).

[57] J. Tersoff, Physical Review B **39**, 5566 (1989).

[58] U. Trinczek and H. Teichler, Physica Status Solidi A **137**, 577 (1993).

[59] W. Weber, Physical Review B **15**, 4789 (1977).

[60] A. S. Nandedkar and J. Narayan, Philosophical Magazine A **61**, 873 (1990).

[61] M. S. Duesbery, B. Joos, and D. J. Michel, Physical Review B **43**, 5143 (1991).

[62] F. H. Stillinger and T. A. Weber, Physical Review B **31**, 5262 (1985).

[63] E. Kaxiras and K. C. Pandey, Physical Review B **38**, 12736 (1988).

Ernest Orlando Lawrence Berkeley National Laboratory
One Cyclotron Road | Berkeley, California 94720

Prepared for the U.S. Department of Energy under Contract No. DE-AC03-76SF00098